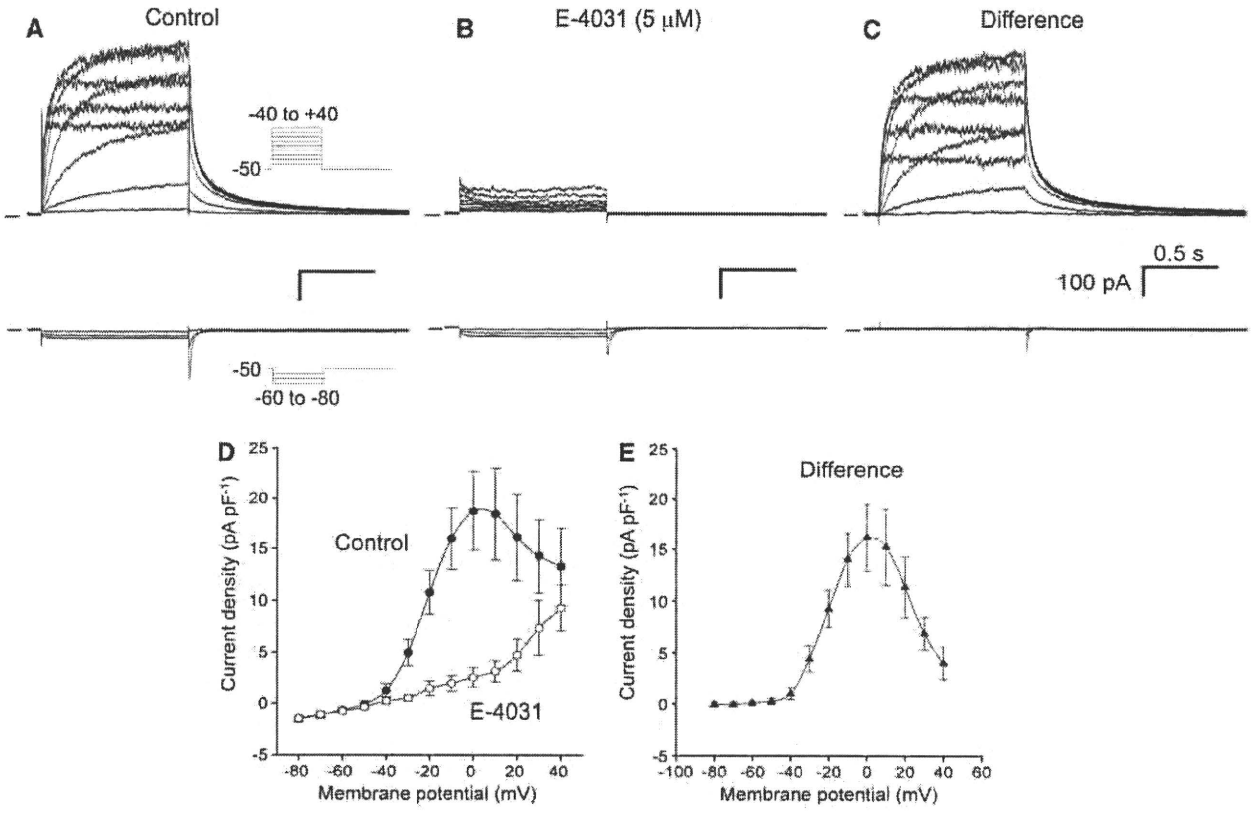

Fig. 1 E-4031-sensitive current recorded from isolated HL-1 cells. **a**, **b** Superimposed whole-cell membrane currents recorded from single HL-1 cell (passage 38) before (**a**) and after (**b**) exposure to 5 μM E-4031. The cell was held at −50 mV and given 1-s depolarizing (between −40 and +40 mV, *upper panel*) and hyperpolarizing (between −80 and −60 mV, *lower panel*) test pulses. The experiment was conducted at 35°C. **c** E-4031-sensitive current obtained from digital subtraction of two traces in **a** and **b**. **d** Average current–voltage relationships recorded before (*filled circles*) and after (*open circles*) exposure to E-4031. Current amplitudes measured just before the end of the 1-s pulses were plotted against the indicated membrane potentials. Values represent mean ± SEM of 10 HL-1 cells (passages 38–41). **e** Current–voltage relationship for E-4031-sensitive currents

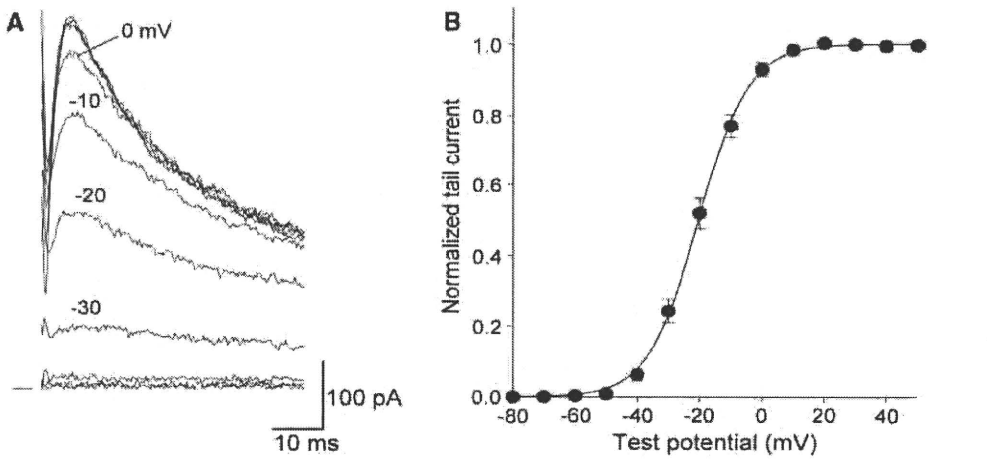

Fig. 2 Voltage-dependent activation of E-4031-sensitive current in HL-1 cells. **a** Representative tails of E-4031-sensitive current recorded from an HL-1 cell (passage 38). Tail currents were elicited on repolarization to −50 mV, following 1-s depolarization to +20 mV. **b** Voltage dependence of E-4031-sensitive current. Tail current amplitudes were normalized to the maximal value at +20 mV, and averaged data were plotted against the indicated test potentials. Values represent mean ± SEM of 10 HL-1 cells (passages 38–41). *Smooth curve* represents fitting of the data to the Boltzmann equation

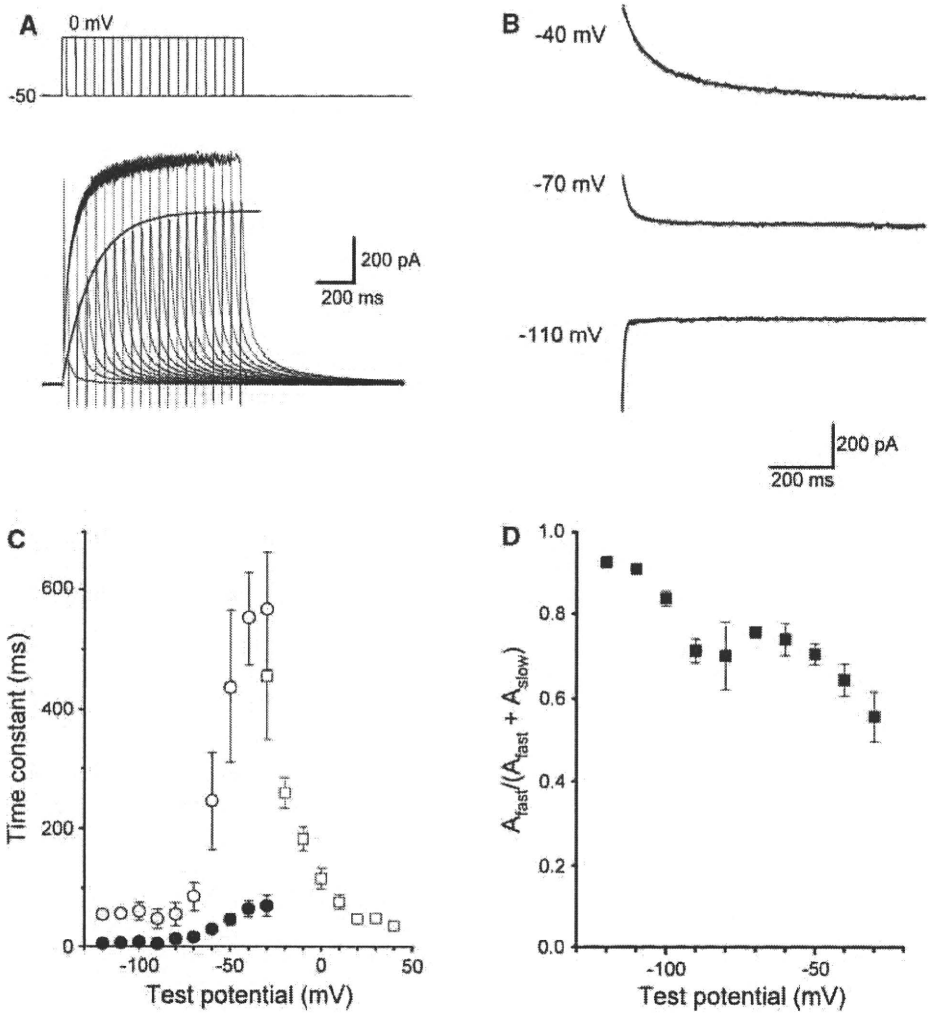

Fig. 3 Activation and deactivation kinetics. **a** Activation time courses assessed with an envelope-of-tails protocol. Original current traces recorded from an HL-1 cell (passage 44) in response to the depolarizing steps to 0 mV of varying duration (25–975 ms in 50-ms increments) from a holding potential of −50 mV. *Solid curve* is a single-exponential fit to the peak tail current elicited upon repolarization to the holding potential. **b** Deactivation time courses of E-4031-sensitive current recorded from an HL-1 cell (passage 39). Decaying phase of tail currents (*dots*) elicited at −40, −70 and −110 mV after depolarizing prepulse to +20 mV of 1-s duration were fit to a sum of two exponential equations (*solid line*). **c** Average voltage dependence of time constants for the apparent activation (*open squares*) and the fast (*open circles*) and slow (*filled circles*) components of deactivation of the E-4031-sensitive current. **d** Voltage dependence of the relative amplitude of the fast component in decaying tail current. Values represent mean ± SEM of four to 10 cells (passages 38–47)

the time course of activation. Figure 3a shows a representative example of current traces in response to depolarizing test pulses to 0 mV of varying duration (25–975 ms in 50-ms increments). The tail current amplitude on return to the holding potential reflects the extent of I_{Kr} activation produced during depolarization to 0 mV, which was well fitted by a single-exponential function, where the τ value was 162.8 ms. The kinetics was steeply voltage-dependent and the activation time constants decreased with incremental changes in the test potentials (τ_{act}, open squares in Fig. 3c). Time constants of deactivation were calculated by fitting the decay of tail currents at various test potentials between −120 and −20 mV following 1-s depolarizing pulses to +20 mV to a double-exponential function, as shown in Fig. 3b. In contrast to activation, the deactivation time course was accelerated at more negative potentials. As summarized in Fig. 3c, both the fast (τ_{fast}, filled circles) and slow (τ_{slow}, open circles) time constants of deactivation were increased as the test potential became more positive. The slow time constants of deactivation at −30 mV were comparable to the time constant of activation at the same potential, and they were plotted as a bell-shaped function of the membrane potential. Figure 3d shows a plot of the relative amplitude of the fast component, $A_{fast}/(A_{fast} + A_{slow})$, of decaying tail current against the membrane potential. The value decreased from approximately 0.9 to 0.5 over the membrane potential from −120 to −20 mV.

I_{Kr} Density in HL-1 Cells

There was a large cell-to-cell variation in HL-1 cell size even in the same culture; C_m measured in patch-clamp experiments ranged between 5.4 and 84.0 pF (mean ± SEM, 29.9 ± 2.3 pF). We tested whether ununiformity of cell size reflects their functional heterogeneity of I_{Kr} channel. The relationship between I_{Kr} density and C_m was investigated in 69 cells (Fig. 4a). The I_{Kr} density ranged between

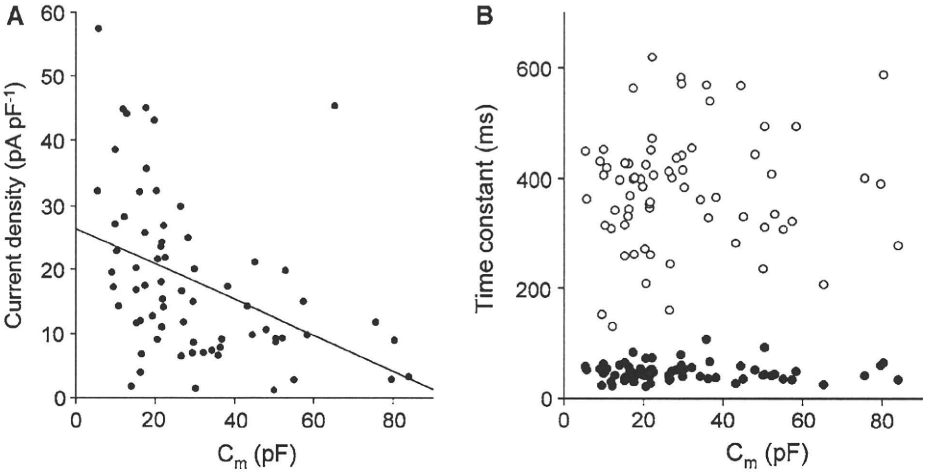

Fig. 4 Relationships between HL-1 cell size and E-4031-sensitive current. Scatter plots of the current density (**a**) and the deactivation time constants (**b**) of the slow (*open circles*) and fast (*filled circles*) components, measured in E-4031-sensitive tail current elicited by a voltage step to −50 mV after 1-s depolarization to +20 mV, against the membrane capacitance of individual cells. Data were obtained from HL-1 cells (passages 38–52)

1.2 and 57.5 pA pF^{-1} (18.1 ± 1.5 pA pF^{-1}, $n = 69$), which was roughly and negatively correlated with cell size ($r = -0.42$, $P < 0.0003$). On the other hand, no obvious correlation between deactivation kinetics of I_{Kr} and cell size was observed (Fig. 4b).

Voltage Dependence of I_{Kr} Inactivation in HL-1 Cells

The shape of the I_{Kr} tail current (initial "hook" or increase in amplitude, followed by slower decay) reflects the presence of a biphasic process during repolarization. The initial increasing phase of the tail current preceding a decay in amplitude has been shown to reflect a recovery from inactivation that occurs much faster than deactivation (Sanguinetti and Jurkiewicz 1990; Shibasaki 1987). In Fig. 5, the rate of recovery from inactivation was estimated. The currents were elicited by voltage pulses to various test potentials between −120 and −10 mV after the 1-s preconditioning pulses to +20 mV. Experiments were conducted at 25°C to allow discrimination of the onset of tail currents from capacitive transients. In Fig. 5a, a set of current traces during test steps is shown. Increment phases of the tail current were well fitted by a single-exponential function with smaller time constants at more negative potentials. For example, the averaged τ value at −120 mV was 0.92 ± 0.04 ms, while it increased to 10.50 ± 0.74 ms at −10 mV (Fig. 5b).

The voltage dependence of current inactivation was examined using a three-pulse protocol (inset in Fig. 6a) (Smith et al. 1996), in which the cell was depolarized to +20 mV for 1 s to activate and inactivate I_{Kr} channels,

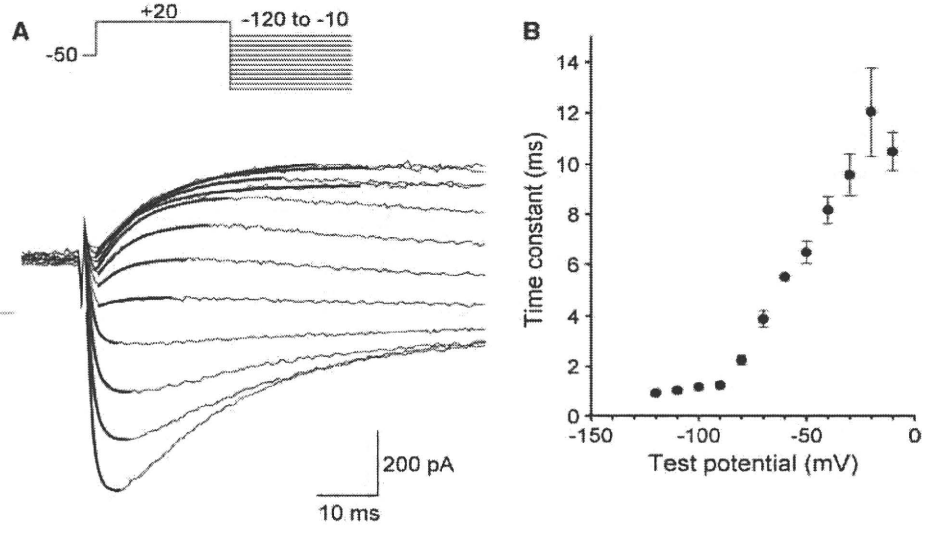

Fig. 5 Kinetic properties of recovery from inactivation. **a** The "hook" tail currents (*thin line*) elicited by voltage steps to various potentials between −120 and −10 mV in 10-mV intervals following the 1-s depolarizing steps to +20 mV (*inset*). Current recording was conducted at 25°C. *Smooth curves* (*thick line*), superimposed to initial increasing phase in amplitude, are obtained by a single-exponential fit. **b** Voltage dependence of the rate of recovery from inactivation. Time constants, measured in (**a**), were plotted against each test potential. Values represent mean ± SEM of four cells (passages 41, 42)

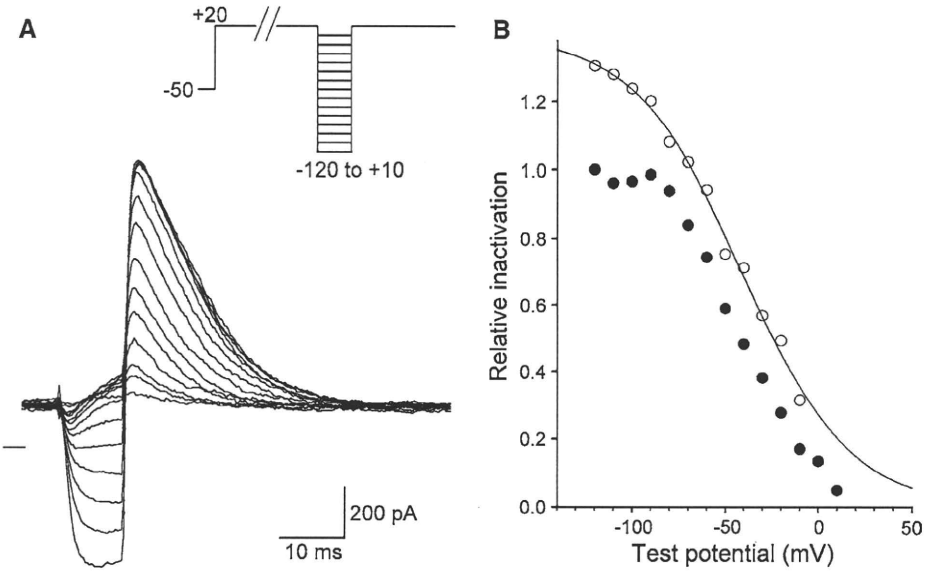

Fig. 6 Voltage dependence of steady-state inactivation. **a** E-4031-sensitive current recorded from an HL-1 cell (passage 41) in response to three-pulse protocol (*inset*). At first, a depolarizing pulse of more than 1 s duration to +20 mV (P1) was applied, where current was activated and inactivated rapidly. Then, a hyperpolarizing test pulse of 10 ms to a varied potential (P2) was used to allow recovery from inactivation, followed by a step to +20 mV (P3). *Dashed line* represents zero current level. Current recording was conducted at 25°C. **b** Current amplitude in response to the P3 pulse (*filled circles*) was normalized to the maximal amplitude at −120 mV and plotted against the test potentials. At negative voltages (≤−60 mV), significant deactivation occurred during 10 ms of the P2 repolarizing step. In addition, at less negative potential (>−70 mV), increasing phase current did not reach the steady-state level during the P2 step. Therefore, the fractional deactivation and incomplete recovery from inactivation during 10 ms were calculated using kinetic parameters (obtained from current traces in Fig. 5), and the data points were corrected to the steady-state inactivation level (*open circles*). Corrected values were well fitted by the Boltzmann equation (*smooth curve*)

then briefly (10 ms) repolarized to various test potentials between −120 and +10 mV to allow for recovery from inactivation without significant deactivation of the channels. After the brief steps, a depolarizing step to +20 mV was applied to evaluate the relative number of opening channels. Figure 6a shows a part of the current traces in response to the pulse protocol (as indicated in the inset). During the brief repolarization, the currents relaxed rapidly to the appropriate level to the corresponding test potentials. Then, depolarizing pulses to +20 mV elicited a large amplitude of outward currents that decayed to the steady-state level within 40 ms due to rapid inactivation. The peak amplitude of the outward currents was measured and plotted against test potentials as filled circles in Fig. 6b. Smith et al. (1996) described that the current amplitude at negative voltages (≤−60 mV) should be corrected because fast deactivation occurred during the brief repolarization. Furthermore, the recovery from inactivation also might not reach the steady-state level at depolarized potential (>−70 mV). Thus, the fractional deactivation and recovery from inactivation during 10-ms repolarizing steps were corrected with respect to the steady-state inactivation level (open circle in Fig. 6b). The half-maximal inactivation voltage calculated by fitting the corrected data to a Boltzmann function was −41.2 mV and the slope factor was 28.9 mV.

K^+ Permeability of I_{Kr} in HL-1 Cells

In Fig. 7, the effects of $[K^+]_o$ on the reversal potential (E_{rev}) of the tail current were investigated. Cells were bathed in Tyrode solution containing 2, 5.4 (normal) and 10 mM KCl; and tail currents were recorded at various test potentials between −120 and 0 mV in 10-mV steps following the 1-s preconditioning pulses to +20 mV (Fig. 7a). The tail current amplitudes were measured and plotted against test potentials in Fig. 7b. At all $[K^+]_o$ conditions, the current–voltage relationships were nearly linear at the potential range between −140 and −80 mV and prominent inward rectification was observed at more positive potential than −70 mV. The conductance at potentials between −140 and −80 mV, measured by fitting lines with a liner regression, was increased with incremental change in $[K^+]_o$ (10.6, 14.1 and 19.7 pS at 2, 5.4 and 10 mM $[K^+]_o$, respectively). E_{rev}, where the polarity of the tail current is reversed, was obtained from a linear regression of the data points between −140 and −70 mV. E_{rev} values at 2, 5.4 and 10 mM $[K^+]_o$ were −115, −91 and −76 mV, respectively, very near the calculated

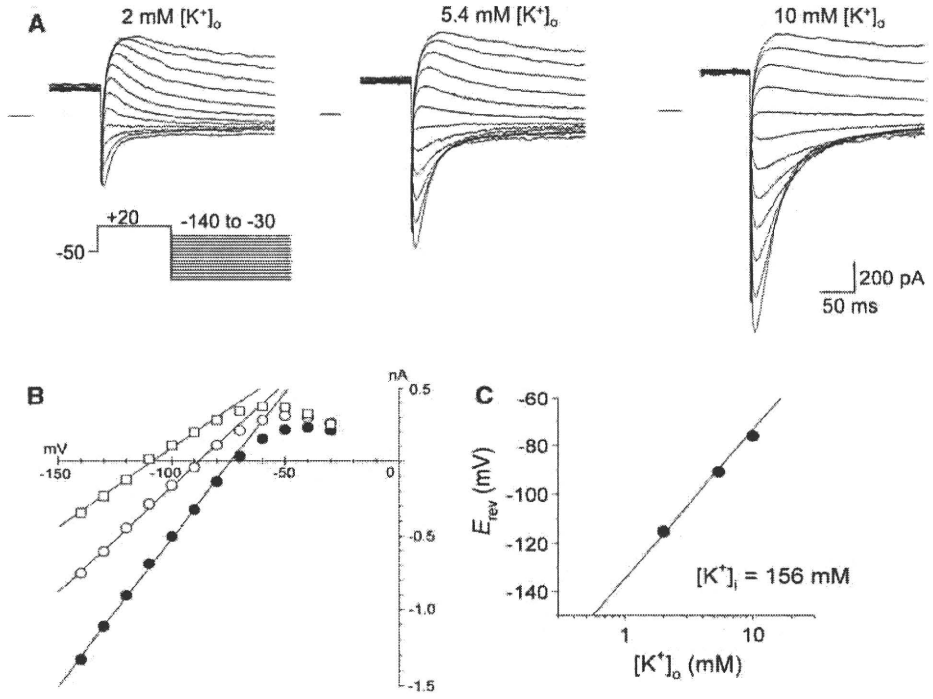

Fig. 7 Effects of extracellular K^+ concentrations on E-4031-sensitive currents. **a** Tail currents recorded at 2 (*left*), 5.4 (*middle*) and 10 mM $[K^+]_o$ conditions (*right*) at 25°C. The cell (passage 39) was initially depolarized to +20 mV from a holding potential of −50 mV, followed by test steps to various potentials between −120 and −30 mV (voltage protocol, *inset*). **b** Tail current amplitude at 2 (*open squares*), 5.4 (*open circles*) and 10 mM $[K^+]_o$ conditions (*filled circles*) shown as a function of test potentials. *Solid lines* on the plot were obtained by a linear regression of data points between −140 and −70 mV: $I_{tail} = g_{max} \cdot (E - E_{rev})$, where g_{max} and E_{rev} were, respectively, 10.6 pS and −115 mV at 2 mM $[K^+]_o$, 14.1 pS and −91 mV at 5.4 mM $[K^+]_o$ and 19.7 pS and −76 mV at 10 mM $[K^+]_o$. **c** Relationships between $[K^+]_o$ and E_{rev}. E_{rev} values in (**b**), plotted against each $[K^+]_o$ concentration, were in good agreement with a predicted E_K (*solid line*) calculated using a Nernst equation, $E_K = RT/F \cdot \ln([K^+]_o/[K^+]_i)$, where $[K^+]_i$ was assumed to be 158 mM

equilibrium potential of K^+ of −116, −89 and −73 mV, respectively (Fig. 7c).

Blocking Effects of E-4031 and Dofetilide on I_{Kr} in HL-1 Cells

In Fig. 8, the blocking effects of methanesulfonanilide drugs E-4031 and dofetilide on I_{Kr} in HL-1 cells were determined. The 1-s depolarizing pulses to +20 mV were repetitively given to the cells every 8 s to activate I_{Kr}, and the blocking effects of the drugs were determined by reduction of tail current elicited at −50 mV. Figure 8a shows the time course of changes in tail current amplitude during application of E-4031 at various concentrations as indicated. In the absence of drugs, the magnitude of the tail current was stable. Exposure to 10 nM E-4031 gradually reduced the tail currents by about 20% at the steady-state level, and the blocking effects increased as the drug concentration became higher. The IC_{50} values for block of tail currents by dofetilide and E-4031 were estimated to be 15.1 and 21.2 nM, respectively; and both drugs inhibited tail current completely at 1 μM (Fig. 8b, c).

Mouse ERG1 Expression Underlies I_{Kr} in HL-1 Cells

In Fig. 9, mERG1 expression in HL-1 cells was investigated with RT-PCR and Western blot assay. It has been reported that there are at least three isoforms of ERG1 at the mRNA level in human and mouse, i.e., the full-length ERG1a and two alternative splicing variants, ERG1a′ and ERG1b, with shorter N termini (Lees-Miller et al. 1997; London et al. 1997). In the present study, therefore, primer pairs directed to each ERG1 isoform were used for PCR amplification. Figure 9a shows an agarose gel of amplified PCR products, where specific bands of the expected size are detected for mERG1a (747 bp), mERG1a′ (755 bp) and mERG1b (1,109 bp) only in the presence of transcriptase. A similar gene expression profile was also detected in adult mouse atrial tissue (Fig. 9b). In order to examine protein expression, we employed an anti-ERG1 antibody that recognizes a common C-terminal epitope in all three mERG1 isoforms. As shown in Fig. 9c, the C-terminal ERG1 antibody identified several bands on a Western blot of HL-1 cells. The two higher bands with molecular mass of 120 and 160 kDa are consistent with maturely

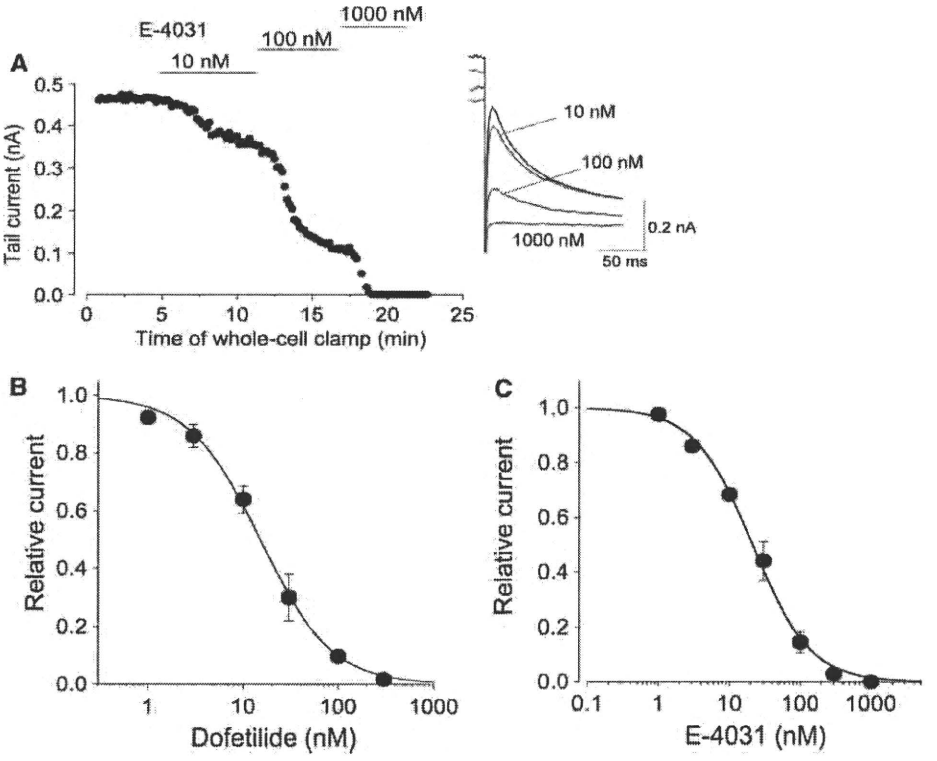

Fig. 8 Inhibitory effects of E-4031 and dofetilide on I_{Kr} in HL-1 cells. **a** Time course of changes in tail current amplitude during exposure to E-4031. Tail currents, as shown in *inset*, were elicited by a voltage step to −50 mV after 1-s depolarization to +20 mV. E-4031 was applied at various concentrations as indicated. **b**, **c** Dose-response relationships of blocking effects of E-4031 (**b**) and dofetilide (**c**). Tail current amplitude was normalized to the maximal amplitude in the absence of drug and plotted against each drug concentration. Data points represent mean ± SEM of five cells (passages 41–52). *Smooth curve* was obtained by fitting the data with a Hill equation, where IC_{50} and Hill coefficient were, respectively, 15.1 nM and 1.2 in (**b**) and 21.2 nM and 1.0 in (**c**)

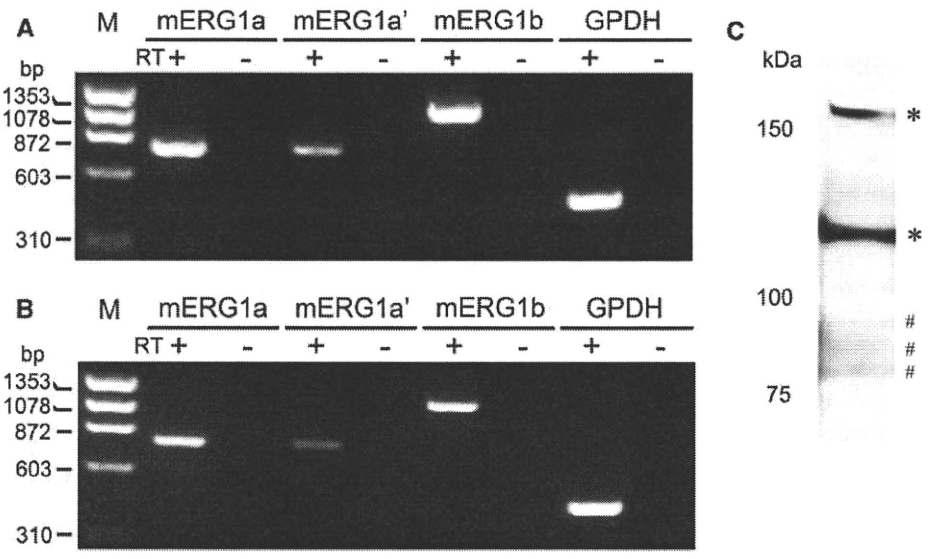

Fig. 9 Expression of mouse ERG1 isoforms in HL-1 cells and mouse atrium. PCR products amplified from cDNA derived from HL-1 cells culture (passage 40) (**a**) and atrial tissues dissected from adult mice (**b**), using primer pairs directed to mERG1a, mERG1a′ or mERG1b. *M* indicates a molecular maker of ϕX174/*Hae*III digest. **c** Western blot of total protein extracts from HL-1 cells (passages 45–47). Blotting with an antibody specific for ERG1 shows two mERG1a glycoform bands (*) at 120 and 160 kDa as well as three mERG1b glycoform bands (#) at 80, 87 and 93 kDa

glycosylated and unglycosylated ERG1a, respectively, in rat and canine ventricular myocytes (Jones et al. 2004), although contamination of signal attributed to ERG1a′ may be possible because of a small difference (~6 kDa) in protein size. On the other hand, we did observe three faint bands with lower molecular mass of 80, 87 and 93 kDa, which are consistent with bands attributed to different glycosylated forms of ERG1b in human and canine ventricular myocytes (Jones et al. 2004) and K562 human leukemic cells (Cavarra et al. 2007).

Recently, gene silencing by RNAi has become a broadly used technology for exploring gene function (Hannon 2002). In the present study, the functional relevance of mERG1 gene expression in HL-1 cells was determined using the RNAi technique. Two siRNA duplex oligonucleotides against all isoforms of mERG1 and ncRNA were

individually transfected into HL-1 cells together with a plasmid vector encoding GFP. Transfection efficacy estimated with green fluorescence was very low (≤5%), which never allowed us to detect an obvious decrease in mERG1 transcripts or proteins at the culture level (data not shown). However, the effects of siRNA were evident in whole-cell membrane current recorded from single GFP-positive cells. Compared to recordings in cells transfected with GFP alone (Fig. 10a), a much smaller time-dependent outward current was observed in cells transfected with siRNA, apparently due to a marked decrease in I_{Kr} amplitude (Fig. 10c, d). The effect of siRNA was attributable to specific knockdown of mERG1 expression because cells transfected with scRNA displayed currents with comparable amplitude to those recorded from cells transfected with GFP alone (Fig. 10b). I_{Kr} density determined by tail current elicited at −50 mV after the 1-s voltage steps to +30 mV was 1.95 ± 0.31 and 1.2 ± 0.34 pA pF^{-1} in cells transfected with siRNA-1 and siRNA-2, respectively. Both values were significantly smaller than those obtained from cells transfected with GFP alone (19.15 ± 2.34 pA pF^{-1}, $P < 0.01$) or with ncRNA (19.00 ± 2.69 pA pF^{-1}, $P < 0.01$) (Fig. 10e).

Discussion

In this article we describe the basic biophysical properties and molecular identity of I_{Kr} channels in HL-1 cells, the unique murine cardiac cell line established by Claycomb et al. (1998). Our current recordings demonstrated that most of the outward conductance in these cells was dominated by E-4031-sensitive current, which exhibited comparable characteristics to I_{Kr} in native mammalian cardiac cells, i.e., voltage- and time-dependent activation, prominent inward rectification, high K^+ permeability and nanomolar sensitivity to dofetilide or E-4031. In addition, we found that HL-1 cells possessed multiple transcripts and

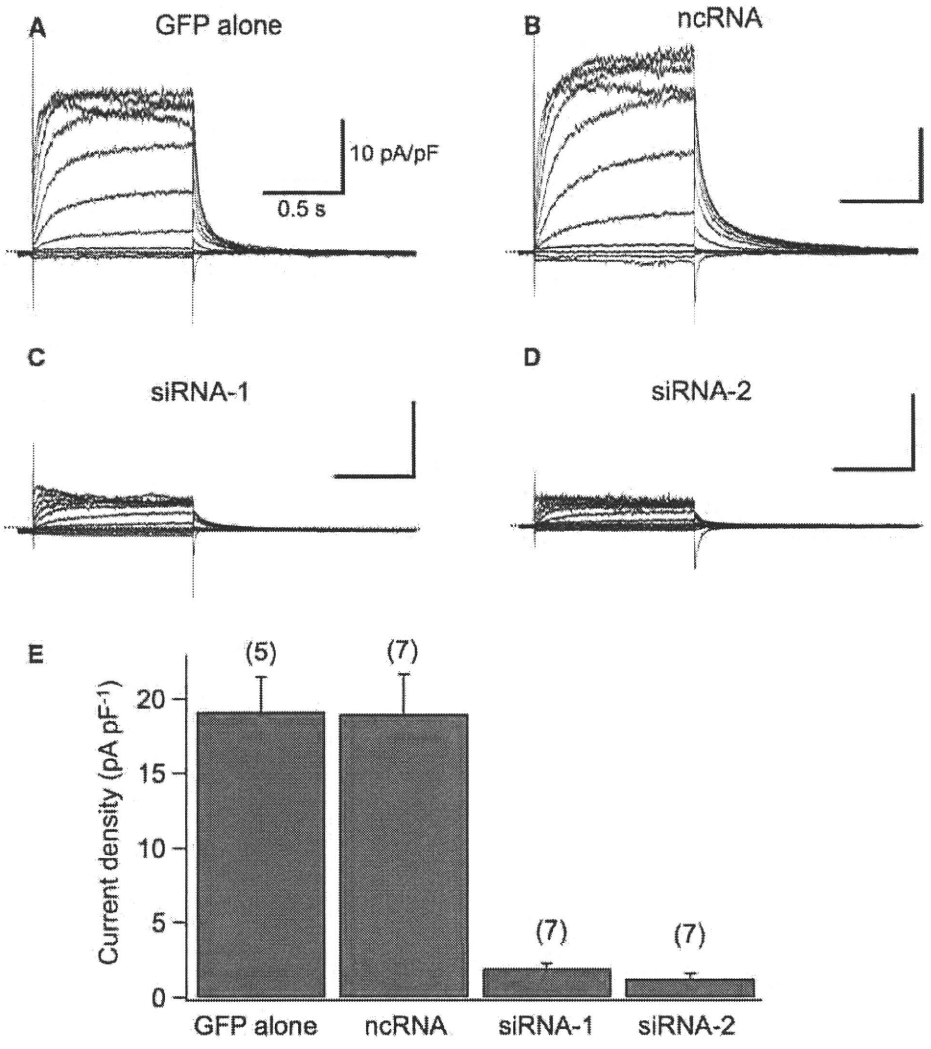

Fig. 10 Knockdown of mouse ERG1 with siRNA in HL-1 cells. Typical current traces recorded from HL-1 cells (passages 40, 41) transfected with GFP alone (**a**), GFP and nonspecific ncRNA (**b**), GFP and siRNA-1 (**c**) and GFP and siRNA-2 (**d**). Cell was held at −50 mV and given 1-s voltage steps to various potentials between −80 mV and +40 mV. **e** Bar graph displaying I_{Kr} density in each group (GFP alone, $n = 5$; GFP plus ncRNA, $n = 7$; GFP plus siRNA-1, $n = 7$; GFP plus siRNA-2, $n = 7$). Tail current was elicited upon repolarization to −50 mV following the 1-s depolarizing steps to +30 mV

proteins for the mouse ERG1 gene, known as molecular candidates underlying I_{Kr}. These findings indicate that HL-1 cells are a preferable source of native I_{Kr} channels.

Biophysical and Pharmacological Properties of I_{Kr} in HL-1 Cells

The biophysical profile of I_{Kr} channels is responsible for their specific role in cardiac action potential. The inward rectification mediated by a rapid voltage-dependent inactivation of channels suppresses current during the depolarizing phase of cardiac action potential, while a rapid recovery from inactivation followed by slow deactivation evokes a resurgent current during phase III repolarization. These unique gating properties have been extensively investigated in HERG channels. However, despite its physiological importance, relatively little information on cardiac I_{Kr} channels is available due to technical difficulties; i.e., significant current magnitude and minimal contamination of other time-dependent K^+ currents are required for reliable measurements. Current recordings in HL-1 cells potentially satisfied these requirements, which allowed us to evaluate the electrophysiological properties of I_{Kr} channels comprehensively. One possible limitation in our I_{Kr} recordings was that a holding potential of −50 mV was used to avoid contamination of $I_{Ca,T}$ (Xia et al. 2004) and I_f (Sartiani et al. 2002), which might affect I_{Kr} kinetic parameters and drug sensitivity because a significant fraction of channels were restrained in the inactivated state at −50 mV (see Fig. 6). Nevertheless, our recordings are similar to ones applying common protocols for the recording of native I_{Kr} in cardiomyocytes; thus, it is possible to draw a comparison between our results and those of earlier studies.

Voltage dependence of I_{Kr} activation in HL-1 cells was determined by two parameters, $V_{1/2}$ of −20.4 mV and k of 8.0 mV, which are practically consistent with the values previously reported for cardiac I_{Kr} in various mammals (Clark et al. 2004; Matsuura et al. 2002; Ono and Ito 1995; Sanguinetti and Jurkiewicz 1990). The deactivation kinetics of I_{Kr} varies between species. It is fast in guinea pig (Sanguinetti and Jurkiewicz 1990), while it is extremely slow in dog and cat (Barajas-Martínez et al. 2000; Liu and Antzelevitch 1995). In the present study, deactivation time constants were 46 ms for τ_{fast} and 438 ms for τ_{slow} at −50 mV when fitted to a double-exponential function, which are very similar to recent observation in mouse SA node cells (τ_{fast} and τ_{slow} were 40–70 ms and 400–600 ms at −50 mV, respectively) (Clark et al. 2004). Recovery from inactivation was very rapid even at 25°C, and time constants obtained in HL-1 cells were comparable to previous data for I_{Kr} in ferret atrial cells (Liu et al. 1996) but considerably smaller than the observation for HERG currents (Sanguinetti et al. 1995). We also determined the voltage dependence of steady-state inactivation of I_{Kr} channels using a three-pulse protocol that has been employed for HERG currents (Smith et al. 1996). The $V_{0.5}$ of −41.2 mV obtained in our analysis was very far from the value with HERG current (−90 mV) (Smith et al. 1996) but relatively similar to the value estimated by other methods in guinea pig or ferret (Liu et al. 1996; Sanguinetti and Jurkiewicz 1990), suggesting fundamental differences between cardiac I_{Kr} and HERG current in inactivation properties. Taken together, HL-1 cells appear to retain species-specific features of native I_{Kr}.

The sensitivity of I_{Kr} in HL-1 cells to E-4031 (IC_{50} 21.1 nM) was similar to that reported for native I_{Kr} in ferret and guinea pig cardiomyocytes (IC_{50} ~10 nM) (Liu et al. 1996; Weerapura et al. 2002). Dofetilide sensitivity observed in the present study (IC_{50} 15.1 nM) was also comparable with the values reported for native I_{Kr} in rabbit and guinea pig cardiomyocytes (IC_{50} 4–9 nM) (Carmeliet 1992; Weerapura et al. 2002). The sensitivity of the HERG channel to these compounds varies among expression systems. The channel expressed in *Xenopus* oocytes displays much lower sensitivity (E-4031 IC_{50} ~1 μM) (Sanguinetti et al. 1995), possibly due to yolk sac absorption of drugs in oocytes (Weerapura et al. 2002). On the other hand, in mammalian cell lines such as HEK cells and CHO cells, the IC_{50} values for the inhibition of HERG channel by E-4031 and dofetilide were reported to be 7.7 and ~10 nM, respectively (Zhou et al. 1998; Weerapura et al. 2002), which are indistinguishable from those previously reported for native I_{Kr} as well as our observation in HL-1 cells. Since inhibition of I_{Kr} is the predominant adverse effect of a diverse range of therapeutic agents (resulting in life-threatening proarrhythmic activity), assay of I_{Kr} in HL-1 cells may serve as a convenient preclinical tool to detect potential arrhythmogenic properties of any compound intended to be used as human medicine.

HL-1 Cells Possess Electrophysiological Properties Resembling Embryonic Phenotypes

Cardiac I_K is known to comprise at least two components, I_{Kr} and I_{Ks}, in various mammals. In HL-1 cells, however, I_{Kr} seems to be the sole I_K component. Indeed, a time-dependent outward current was almost totally abolished by application of E-4031 (Fig. 1). In mouse ventricular myocytes, the expression level of I_{Kr} and I_{Ks} is dependent on the developmental stage (Wang and Duff 1996; Wang et al. 1996); i.e., I_{Kr} is the predominant component of I_K in embryonic and fetal mice but is decreased during early postnatal development, whereas I_{Ks} is increased and both currents almost disappear in adult mouse. Along with these finding, the I_{Kr} expression pattern of HL-1 cells appears to

be similar to that of immature fetal mouse myocytes rather than well-differentiated adult mouse myocytes, although they derived from adult mouse hearts. Similarly, a fetal-type electrophysiological phenotype of HL-1 cells has been indicated by the expression of I_f and $I_{Ca,T}$ (Sartiani et al. 2002; Xia et al. 2004), which are known to be manifested in ventricular myocytes only at early embryonic stages (Niwa et al. 2004; Yasui et al. 2001).

HL-1 cells are known to beat when grown at proper density, again resembling embryonic cardiomyocytes. The spontaneous contractile activity, however, occurs in a restricted region of culture (Sartiani et al. 2002), suggesting heterogeneity of the functional expression level of ion channels in HL-1 cells. In fact, I_f was observed in only ~30% of HL-1 cells (Sartiani et al. 2002). Interestingly, the presence of both $I_{Ca,L}$ and $I_{Ca,T}$ had similar incidence (Xia et al. 2004). The limited expression of these membrane currents seems to be in agreement with the partial (local) occurrence of spontaneous beating in HL-1 cell culture because they play crucial roles in cardiac pacemaker activity. In the present study, I_{Kr} was recorded in almost all cells tested, even in quiescent HL-1 cells, while the current density of I_{Kr} was roughly and significantly correlated with cell size (Fig. 4). It has been suggested that a cell size-dependent difference in expression level of various ionic currents underlies the regional difference in electrical activity of rabbit SA node (Honjo et al. 1996; Lei et al. 2001). Although the relationship between spontaneous activity and the size of HL-1 cells is not known, it may be that the expression level of I_{Kr} channels is involved in the capability of spontaneous beating in HL-1 cell culture.

Molecular Basis of I_{Kr} in HL-1 Cells

The molecular basis of native I_{Kr} channel is still in debate. Although there is little doubt that the ERG1 gene underlies I_{Kr} channels in the heart, the reconstituted HERG channel displays much slower deactivation kinetics than native I_{Kr} channels (Sanguinetti et al. 1995). For this reason, auxiliary subunits such as KCNE1 and KCNE2 have been implicated as functional regulators of HERG channel (Abbott et al. 1999; McDonald et al. 1997). According to our preliminary experiments, we detected mRNA for KCNE1 from HL-1 cells, consistent with previous observations in AT-1 cells (Yang et al. 1994), but failed to find obvious expression of KCNE2 (data not shown). On the other hand, N-terminal splice variants of the ERG1 gene have been cloned in mouse and human and suggested to generate functional diversity of native I_{Kr} channels (Lees-Miller et al. 1997; London et al. 1997). The importance of these variants in the human heart was recently highlighted by the finding of a HERG1b-specific missense mutation associated with long QT syndrome (Sale et al. 2008). The N-terminal region of ERG1 contains the Per-Arnt-Sim (PAS) domain, which plays a crucial role in the slow deactivation process of the channel (Morais Cabral et al. 1998). The ERG1b isoform, which lacks the PAS domain in its truncated N terminus, exhibits faster deactivation than the full-length ERG1a (London et al. 1997), although its surface expression is not efficient unless coassembled with ERG1a (Phartiyal et al. 2007). In heterologous systems, coexpression of ERG1a and ERG1b leads to formation of a functional heterotetrameric channel with deactivation properties that more closely resemble native I_{Kr} than the channels produced by the expression of these isoforms individually (London et al. 1997). In fact, the deactivation time course of I_{Kr} in HL-1 cells was more similar to that reported for the mERG1a/1b channels rather than the mERG1a homomeric channel (e.g., τ_{fast} and τ_{slow} at -50 mV were 46 and 438 ms, respectively, in our experiments compared to 400–500 and ~2,000 ms, respectively, in mERG1a channel and 70–80 and 400–600 ms, respectively, in mERG1a/1b channel [London et al. 1997]). In the present study, we also confirmed the expression of both mERG1a and mERG1b in HL-1 cells, supporting the possible contribution of these isoforms in producing I_{Kr} in HL-1 cells. However, despite the abundance of transcripts, the protein bands for mERG1b were much weaker than those for mERG1a in our immunoblot analysis using an antibody that recognizes the common C-terminal epitope in both isoforms (Fig. 9). This might be attributable to differential accessibility of antibody to the common epitope in mERG1a and mERG1b (Jones et al. 2004). In mammalian heart, ERG1b protein expression has been clearly demonstrated using an isoform-specific antibody (Jones et al. 2004), whereas the antibodies against a common epitope recognized only ERG1a protein but failed to detect ERG1b (Pond et al. 2000). Further experiments are required to clarify the relative contribution of the mERG1b isoform to the generation of I_{Kr} in HL-1 cells.

Recently, siRNA has proven to be a powerful tool for investigating gene function by inducing knockdown phenotypes (Hannon 2002). In the present study, siRNA-mediated knockdown of mERG1 resulted in a dramatic decrease in I_{Kr}, providing direct evidence for an essential role of the mERG1 gene in the generation of I_{Kr} in HL-1 cells. It is possible to design siRNA for each isoform of mERG1 by targeting a specific exon sequence. Thus, our siRNA experiments suggested its potential application to the identification of gene products responsible for forming I_{Kr} in HL-1 cells. A major limitation of this approach was the difficulty of siRNA delivery into HL-1 cells. Our transfection efficiency using cationic lipids was <5%, which was sufficient for patch-clamp study but inadequate for biochemical analysis including measurements of mRNA and protein levels.

HL-1 Cells Are a More Reliable Source of I_{Kr} than AT-1 Cells

The electrophysiological characteristics of HL-1 cells seem to be qualitatively similar to those previously reported in their progenitor, AT-1 cells (Yang et al. 1994), except that the I_{Kr} density obtained from HL-1 cells in the present study (18 pA pF^{-1}) is three to four times larger than the value reported for AT-1 cells ($\sim$5 pA pF^{-1}) (Yang et al. 1994). Most importantly, they are quite different in their growth in culture. AT-1 cells proliferate to some extent in vitro, while extremely increasing their cell size, which is accompanied by changes in I_{Kr} density during primary culture (Yang et al. 1995). On the contrary, HL-1 cells can divide indefinitely in culture, while retaining their phenotype during continuous passages (Claycomb et al. 1998). In conclusion, taking advantage of their proliferative ability and stability of phenotype in culture, HL-1 cells can be adapted not only for electrophysiological experiments but also for biochemical and molecular biological experiments that require long-term culturing and provide a useful cardiac model for studies on the gating mechanisms, regulation by various signaling pathways, drug block and molecular basis of native I_{Kr} channels.

Acknowledgements This study was supported by a Grant-in Aid for Scientific Research from the Japan Society for the Promotion of Science. We are grateful to Dr. W. C. Claycomb for providing HL-1 cells.

References

Abbott GW, Sesti F, Splawski I et al (1999) MiRP1 forms I_{Kr} potassium channels with HERG and is associated with cardiac arrhythmia. Cell 97:175–187

Barajas-Martínez H, Elizalde A, Sánchez-Chapula JA (2000) Developmental differences in delayed rectifying outward current in feline ventricular myocytes. Am J Physiol 278:H484–H492

Carmeliet E (1992) Voltage- and time-dependent block of the delayed K^+ current in cardiac myocytes by dofetilide. J Pharmacol Exp Ther 262:809–817

Cavarra MS, del Mónaco SM, Assef YA et al (2007) HERG currents in native K562 leukemic cells. J Membr Biol 219:49–61

Chomczynski P, Sacchi N (1987) Single-step method of RNA isolation by acid guanidinium thiocyanate-phenol-chloroform extraction. Anal Biochem 162:156–159

Clark RB, Mangoni ME, Lueger A et al (2004) A rapidly activating delayed rectifier K^+ current regulates pacemaker activity in adult mouse sinoatrial node cells. Am J Physiol 286:H1757–H1766

Claycomb WC, Lanson NA Jr, Stallworth BS et al (1998) HL-1 cells: a cardiac muscle cell line that contracts and retains phenotypic characteristics of the adult cardiomyocyte. Proc Natl Acad Sci USA 95:2979–2984

Curran ME, Splawski I, Timothy KW et al (1995) A molecular basis for cardiac arrhythmia: *HERG* mutations cause long QT syndrome. Cell 80:795–803

Delcarpio JB, Lanson NA Jr, Field LJ et al (1991) Morphological characterization of cardiomyocytes isolated from a transplantable cardiac tumor derived from transgenic mouse atria (AT-1 cells). Circ Res 69:1591–1600

Field LJ (1988) Atrial natriuretic factor-SV40 T antigen transgenes produce tumors and cardiac arrhythmias in mice. Science 239:1029–1033

Hamill OP, Marty A, Neher E et al (1981) Improved patch-clamp techniques for high-resolution current recording from cells and cell-free membrane patches. Pflugers Arch 391:85–100

Hannon GJ (2002) RNA interference. Nature 418:244–251

Honjo H, Boyett MR, Kodama I et al (1996) Correlation between electrical activity and the size of rabbit sino-atrial node cells. J Physiol 496:795–808

Jones EM, Roti Roti EC, Wang J et al (2004) Cardiac I_{Kr} channels minimally comprise hERG 1a and 1b subunits. J Biol Chem 279:44690–44694

Lees-Miller JP, Kondo C, Wang L et al (1997) Electrophysiological characterization of an alternatively processed ERG K^+ channel in mouse and human hearts. Circ Res 81:719–726

Lei M, Honjo H, Kodama I et al (2001) Heterogeneous expression of the delayed-rectifier K^+ currents $i_{K,r}$ and $i_{K,s}$ in rabbit sinoatrial node cells. J Physiol 535:703–714

Liu DW, Antzelevitch C (1995) Characteristics of the delayed rectifier current (I_{Kr} and I_{Ks}) in canine ventricular epicardial, midmyocardial, and endocardial myocytes. A weaker I_{Ks} contributes to the longer action potential of the M cell. Circ Res 76:351–365

Liu Y, Taffet SM, Anumonwo JM et al (1994) Characterization of an E4031-sensitive potassium current in quiescent AT-1 cells. J Cardiovasc Electrophysiol 5:1017–1030

Liu S, Rasmusson RL, Campbell DL et al (1996) Activation and inactivation kinetics of an E-4031-sensitive current from single ferret atrial myocytes. Biophys J 70:2704–2715

London B, Trudeau MC, Newton KP et al (1997) Two isoforms of the mouse *ether-a-go-go*-related gene coassemble to form channels with properties similar to the rapidly activating component of the cardiac delayed rectifier K^+ current. Circ Res 81:870–878

Matsuura H, Ehara T, Ding WG et al (2002) Rapidly and slowly activating components of delayed rectifier K^+ current in guinea-pig sino-atrial node pacemaker cells. J Physiol 540:815–830

McDonald TV, Yu Z, Ming Z et al (1997) A minK-HERG complex regulates the cardiac potassium current I_{Kr}. Nature 388:289–292

McWhinney CD, Hansen C, Robishaw JD (2000) Alpha-1 adrenergic signaling in a cardiac murine atrial myocyte (HL-1) cell line. Mol Cell Biochem 214:111–119

Morais Cabral JH, Lee A, Cohen SL et al (1998) Crystal structure and functional analysis of the HERG potassium channel N-terminus: a eukaryotic PAS domain. Cell 95:649–655

Neilan CL, Kenyon E, Kovach MA et al (2000) An immortalized myocyte cell line, HL-1, expresses a functional δ-opioid receptor. J Mol Cell Cardiol 32:2187–2193

Niwa N, Yasui K, Opthof T et al (2004) $Ca_v3.2$ subunit underlies the functional T-type Ca^{2+} channel in murine hearts during the embryonic period. Am J Physiol 286:H2257–H2263

Ono K, Ito H (1995) Role of rapidly activating delayed rectifier K^+ current in sinoatrial node pacemaker activity. Am J Physiol 269:H453–H462

Phartiyal P, Jones EMC, Robertson GA (2007) Heteromeric assembly of human ether-à-go-go-related gene (hERG) 1a/1b channels occurs cotransfectionally via N-terminal interactions. J Biol Chem 282:9874–9882

Pond AL, Scheve BK, Benedict AT et al (2000) Expression of distinct ERG proteins in rat, mouse, and human heart. Relation to functional I_{Kr} channels. J Biol Chem 275:5997–6006

Roden DM, Lazzara R, Rosen M et al (1996) Multiple mechanisms in the long-QT syndrome. Current knowledge, gaps, and future directions. The SADS Foundation Task Force on LQTS. Circulation 94:1996–2012

Sale H, Wang J, O'Hara TJ et al (2008) Physiological properties of hERG 1a/1b heteromeric currents and a hERG 1b-specific mutation associated with long-QT syndrome. Circ Res 103: e81–e95

Sanguinetti MC, Jurkiewicz NK (1990) Two components of cardiac delayed rectifier K^+ current. Differential sensitivity to block by class III antiarrhythmic agents. J Gen Physiol 96:195–215

Sanguinetti MC, Jiang C, Curran ME et al (1995) A mechanistic link between an inherited and an acquired cardiac arrhythmia: *HERG* encodes the I_{Kr} potassium channel. Cell 81:299–307

Sartiani L, Bochet P, Cerbai E et al (2002) Functional expression of the hyperpolarization-activated, non-selective cation current I_f in immortalized HL-1 cardiomyocytes. J Physiol 545:81–92

Shibasaki T (1987) Conductance and kinetics of delayed rectifier potassium channels in nodal cells of the rabbit heart. J Physiol 387:227–250

Smith PL, Baukrowitz T, Yellen G (1996) The inward rectification mechanism of the HERG cardiac potassium channel. Nature 379:833–836

Trudeau MC, Warmke JW, Ganetzky B et al (1995) HERG, a human inward rectifier in the voltage-gated potassium channel family. Science 269:92–95

Wang L, Duff HJ (1996) Identification and characteristics of delayed rectifier K^+ current in fetal mouse ventricular myocytes. Am J Physiol 270:H2088–H2093

Wang L, Feng ZP, Kondo CS et al (1996) Developmental changes in the delayed rectifier K^+ channels in mouse heart. Circ Res 79:79–85

Weerapura M, Nattel S, Chartier D et al (2002) A comparison of currents carried by HERG, with and without coexpression of MiRP1, and the native rapid delayed rectifier current. Is MiRP1 the missing link? J Physiol 540:15–27

White SM, Constantin PE, Claycomb WC (2004) Cardiac physiology at the cellular level: use of cultured HL-1 cardiomyocytes for studies of cardiac muscle cell structure and function. Am J Physiol 286:H823–H829

Xia M, Salata JJ, Figueroa DJ et al (2004) Functional expression of L- and T-type Ca^{2+} channels in murine HL-1 cells. J Mol Cell Cardiol 36:111–119

Yang T, Roden DM (1996) Extracellular potassium modulation of drug block of I_{Kr}. Implications for torsade de pointes and reverse use-dependence. Circulation 93:407–411

Yang T, Wathen MS, Felipe A et al (1994) K^+ currents and K^+ channel mRNA in cultured atrial cardiac myocytes (AT-1 cells). Circ Res 75:870–878

Yang T, Kupershmidt S, Roden DM (1995) Anti-minK antisense decreases the amplitude of the rapidly activating cardiac delayed rectifier K^+ current. Circ Res 77:1246–1253

Yang T, Snyders DJ, Roden DM (1997) Rapid inactivation determines the rectification and $[K^+]_o$ dependence of the rapid component of the delayed rectifier K^+ current in cardiac cells. Circ Res 80:782–789

Yasui K, Liu W, Opthof T et al (2001) I_f current and spontaneous activity in mouse embryonic ventricular myocytes. Circ Res 88:536–542

Zankov DP, Yoshida H, Tsuji K et al (2009) Adrenergic regulation of the rapid component of delayed rectifier K^+ current: implications for arrhythmogenesis in LQT2 patients. Heart Rhythm 6:1038–1046

Zhou Z, Gong Q, Ye B et al (1998) Properties of HERG channels stably expressed in HEK 293 cells studied at physiological temperature. Biophys J 74:230–241

Circulation Journal
Official Journal of the Japanese Circulation Society
http://www.j-circ.or.jp

ORIGINAL ARTICLE
Arrhythmia/Electrophysiology

Atrioventricular Block-Induced Torsades de Pointes With Clinical and Molecular Backgrounds Similar to Congenital Long QT Syndrome

Yuko Oka, MD; Hideki Itoh, MD, PhD; Wei-Guang Ding, MD, PhD; Wataru Shimizu, MD, PhD; Takeru Makiyama, MD, PhD; Seiko Ohno, MD, PhD; Yukiko Nishio, MD; Tomoko Sakaguchi, MD, PhD; Akashi Miyamoto, MD; Mihoko Kawamura, MD; Hiroshi Matsuura, MD, PhD; Minoru Horie, MD, PhD

Background: Atrioventricular block (AVB) sometimes complicates QT prolongation and torsades de pointes (TdP).

Methods and Results: The clinical and genetic background of 14 AVB patients (57±21 years, 13 females) who developed QT prolongation and TdP was analyzed. Electrophysiological characteristics of mutations were analyzed using heterologous expression in Chinese hamster ovary cells, together with computer simulation models. Every patient received a pacemaker or implantable cardioverter defibrillator; 3 patients had recurrence of TdP during follow-up because of pacing failure. Among the ECG parameters, QTc interval was prolonged to 561±76 ms in the presence of AVB, but shortened to 495±42 ms in the absence of AVB. Genetic screening for *KCNQ1*, *KCNH2*, *SCN5A*, *KCNE1*, and *KCNE2* revealed four heterozygous missense mutations of *KCNQ1* or *KCNH2* in 4 patients (28.6%). Functional analyses showed that all mutations had loss of functions and various gating dysfunctions of I_{Ks} or I_{Kr}. Finally, action potential simulation based on the Luo-Rudy model demonstrated that most mutant channels induced bradycardia-related early afterdepolarizations.

Conclusions: Incidental AVB, as a trigger of TdP, can manifest as clinical phenotypes of long QT syndrome (LQTS), and that some patients with AVB-induced TdP share a genetic background with those with congenital LQTS. (*Circ J* 2010; **74:** 2562–2571)

Key Words: Atrioventricular block; Ion channels; Long QT syndrome; Torsades de pointes

The acquired form of long QT syndrome (LQTS) is a major cause of torsades de pointes (TdP),[1,2] which results from various factors, including drugs, bradycardia or hypokalemia. Regarding bradycardia, Kurita et al demonstrated that patients with bradycardia-induced TdP display abnormally prolonged QT intervals at slower heart rates (<60 beats/min) than those without TdP.[3] Some groups have reported the genetic background of bradycardia-induced TdP, as well as of congenital LQTS. In 2001, we reported a female with 2:1 atrioventricular block (AVB) and TdP, in whom the *KCNH2* A490T mutant was identified as heterozygous.[4] Subsequently, Lupoglazoff et al demonstrated that, in neonates, LQTS with 2:1 AVB is associated with *KCNH2* mutations whereas sinus bradycardia-related LQTS is associated with *KCNQ1* mutations.[5] Chevalier et al reported that among 29 patients with complete AVB and a QT interval >600 ms, 5 (17%) had mutations on genes encoding K^+ channels, and the expression test of these mutations showed functional changes compared with the wild-type (WT) K^+ current.[6]

Editorial p 2546

In Japan, some papers on congenital LQTS have been published,[2,7–9] but the molecular pathogenesis of AVB-related TdP has not been fully examined, particularly with respect to the relationship between genotype and cellular electrophysiology. The aim of this study was to investigate gene mutations and clarify their functional outcome in con-

Received May 31, 2010; revised manuscript received July 30, 2010; accepted August 2, 2010; released online October 21, 2010 Time for primary review: 16 days

Department of Respiratory and Cardiovascular Medicine (Y.O., H.I., T.S., A.M., M.K., M.H.), Department of Physiology (W.-G.D., H.M.), Shiga University of Medical Science, Otsu; Division of Cardiology, Division of Arrhythmia and Electrophysiology, Department of Cardiovascular Medicine, National Cerebral and Cardiovascular Center, Suita (W.S.); and Department of Cardiovascular Medicine, Kyoto University Graduate School of Medicine, Kyoto (T.M., S.O., Y.N.), Japan

Mailing address: Minoru Horie, MD, PhD, Department of Respiratory and Cardiovascular Medicine, Shiga University of Medical Science, Seta Tsukinowa-cho, Otsu 520-2192, Japan. E-mail: horie@belle.shiga-med.ac.jp

ISSN-1346-9843 doi:10.1253/circj.CJ-10-0498

secutive AVB patients complicated with TdP.

Methods

Study Population

The study cohort contained 14 consecutive probands, from unrelated families, who showed a prolonged QT interval and TdP associated with AVB. They were referred to 3 institutes in Japan; Shiga University of Medical Science (Otsu), National Cardiovascular Center (Suita), and Kyoto University Graduate School of Medicine (Kyoto) for LQTS genetic testing between 1996 and 2008.

Clinical Characterization

In each case, we recorded 12-lead electrocardiograms (ECGs) before and after AVB episodes, as well as gathering the results from other cardiovascular examinations and detailed clinical evaluations. Prolonged QT interval was diagnosed by the presence of prolongation of ventricular repolarization (corrected QT interval [QTc] >460 ms in lead V_5, according to Bazett's formula).[10] We excluded cases of TdP caused by AVB with drugs associated with QT prolongation, as well as those with active ischemia detected by noninvasive or invasive tests, including coronary angiography. We also investigated cardiac events in all 14 probands and their family members. Cardiac events were syncope, TdP, ventricular fibrillation (VF), aborted cardiac arrest (requiring defibrillation) or sudden cardiac death. We also followed the therapies and clinical prognoses of these patients.

Genetic Analysis

Genomic DNA was isolated from venous blood by QIAamp DNA blood midikit (Qiagen, Hilden, Germany). Established primer settings were used to amplify the entire coding regions of the known LQTS genes (*KCNQ1*, *KCNH2*, *SCN5A*, *KCNE1*, and *KCNE2*). Denaturing high-performance liquid chromatography (WAVE system Model 3500, Transgenomic, Omaha, NE, USA) was performed as described elsewhere, and abnormal conformers were amplified by polymerase chain reaction (PCR), and sequenced with an ABI PRISM-3130 sequencer (Perkin-Elmer Applied Biosystems, Wellesley, MA, USA). If we detected mutations in these genes, family members associated with the probands were also genetically analyzed. Formal informed consent was obtained from each patient or their guardians according to standards approved by local institutional review boards.

Expression Plasmids

The expression plasmids, pIRES2-EGFP/*KCNQ1*(wild-type; WT/*KCNQ1*) and pRc-CMV/*KCNH2* (WT/*KCNH2*) were kindly provided by Dr Barhanin (Université de Nice, Sophia Antipolis, Valbonne, France) and Dr Sanguinetti (University of Utah, Salt Lake City, UT, USA), respectively. The mutations were introduced using overlap PCR. The mutant plasmids were constructed by substituting the 838-bp *Xho*I-*Bgl*II for the G272V mutant, 464-bp *Hin*dIII-*Bst*XI for the D111V mutant, 1458-bp *Bst*XI-*Bgl*II for the A490T mutant, or 592-bp *Fse*I-*Sbf*I fragments for the P846T mutant for the corresponding fragments of WT/*KCNQ1* or WT/*KCNH2*. The nucleotide sequence of the construct was confirmed prior to the expression studies.

Expression in Chinese Hamster Ovary (CHO) Cells

CHO cells were maintained in Dulbecco's modified Eagle's medium and Ham's F12 nutritional mixture (Gibco-BRL, Rockville, MD, USA) supplemented with 10% fetal bovine serum (Gibco-BRL) and antibiotics (100 U/ml penicillin and 100 μg/ml streptomycin) in a humidified incubator gassed with 5% CO_2 and 95% air at 37°C. CHO cells were transiently transfected using 1 μg of WT/*KCNQ1* or mutant/*KCNQ1*, and 1 μg of pIRES-CD8/*KCNE1* per 35-mm dish, using the LipofectAMINE method according to the manufacturer's instructions (Invitrogen, Carlsbad, CA, USA). In some experiments, 0.5 μg of WT/*KCNQ1* was transfected with or without mutant/*KCNQ1*, instead of 1 μg of WT/*KCNQ1*. Cells successfully transfected with both *KCNQ1* and *KCNE1* cDNA were selected by green fluorescent protein (GFP) and decoration with anti-CD8 antibody-coated beads (Dynabeads CD8; Dynal Biotech, Oslo, Norway). The cells were transiently transfected with either WT/*KCNH2* or mutant/*KCNH2*, using the LipofectAMINE method according to the manufacturer's instructions. For a 35-mm dish the amount of plasmid was 2 μg and 0.175 μg of GFP; only GFP-positive cells were used for the patch-clamp study.

Electrophysiological Experiments

Whole-cell patch-clamp recordings were conducted at 37.0±1.0°C using an EPC-8 patch-clamp amplifier (HEKA, Lambrecht, Germany) 48–72 h after transfection. No leak subtraction was used. The normal Tyrode solution contained (in mmol/L): NaCl 140, KCl 5.4, $CaCl_2$ 1.8, $MgCl_2$ 0.5, NaH_2PO_4 0.33, glucose 5.5, and HEPES 5 (pH adjusted to 7.4 with NaOH). The pipette solution contained (in mmol/L): potassium aspartate 70, KCl 40, KH_2PO_4 10, EGTA 5, $MgSO_4$ 1, Na_2-ATP (Sigma, St Louis, MO, USA) 3, Li_2-GTP 0.1, and HEPES 5 (pH adjusted to 7.4 with KOH). A coverslip with adherent CHO cells was placed on the bottom of a glass recording chamber (0.5 ml in volume) mounted on the stage of an inverted microscope (TE2000-U, Nikon, Tokyo, Japan). Pipette resistance was 3–5 MΩ when filled with internal solution. Currents and voltages were digitized and voltage commands were generated through an LIH-1600 AD/DA interface (HEKA) controlled by PatchMaster software (HEKA). Current amplitude was divided by membrane capacitance (Cm) to obtain current densities (pA/pF) in each cell. The voltage-dependence of current activation was determined by fitting the normalized tail current (I_{tail}) vs test potential (V_{test}) to a Boltzmann function:

$$I_{tail} = 1/(1+\exp[(V_{0.5}-V_t)/k]),$$

where $V_{0.5}$ indicates the voltage at which the current is half-maximally activated and k is the slope factor.

Computer Simulation of Action Potential Duration (APD)

Ventricular action potentials were simulated by using the dynamic Luo-Rudy model with recent modifications.[11,12] The ratio of I_{Kr} and I_{Ks} conductance was set at 23:1, 17:1, and 19:1 in the epicardium, endocardium, and M cell layer, respectively. Based on the experimental data of voltage-clamp recordings of *KCNH2* channels heterologously expressed in CHO cells, we constructed Markov or Hodgkin-Huxley models for simulated mutant channels as compared with mutants associated with congenital LQTS. In order to construct mutant channel models, we decreased the conductance of each channel as appropriate for the decreased current density, and looked for adequate changes in mutant channels by changing each coefficient value, in turn, for gating states associated with impaired gating defects. The simulation for voltage-clamp experiments was calculated using the 4th-order Runge-Kutta method with a fixed-time step of

Table 1. Clinical Characteristics and Gene Mutations of Probands With Bradycardia-Induced Torsades de Pointes

Case no.	Age (years)	Sex (M/F)	Diagnosis	Cardiac events	Family history	ECG at AVB		ECG without AVB		Therapy	Follow-up		Mutation/Gene
						QTc (ms)	HR (beats/min)	QTc (ms)	HR (beats/min)		Period (months)	Arrhythmic events	
1	27	F	2:1 AVB	TdP	–	600	50	545	71	PM	41	None	A490T/KCNH2
2	74	F	CAVB	TdP	–	NA	NA	NA	NA	PM	22	None	
3	73	M	CAVB	TdP	–	635	39	NA	NA	PM	104	None	
4	57	F	CAVB	TdP	–	525	43	545	61	ICD, BB, Ib	96	None	D111V/KCNH2
5	69	F	2:1 AVB	TdP	–	452	45	476	86	PM, BB, Ib	84	None	
6	21	F	Wenckebach AVB	TdP	Sudden death	625	65	489	75	ICD, Ib	79	VF because of Wenckebach AVB	
7	76	F	2:1 AVB	TdP	–	578	50	424	83	PM, BB	59	None	G272V/KCNQ1
8	71	F	CAVB	TdP	–	729	57	489	72	ICD	46	None	P846T/KCNH2
9	73	F	CAVB	TdP	–	567	33	NA	NA	PM	129	None	
10	62	F	CAVB	TdP	–	473	29	NA	NA	PM	277	None	
11	68	F	CAVB	TdP	–	552	39	NA	NA	PM	207	TdP because of V pacing failure	
12	38	F	CAVB	TdP	Mother with LQTS	493	28	500	65	PM, BB	NA	NA	
13	76	F	CAVB	TdP	–	500	46	NA	NA	PM	57	TdP because of low back-up rate	
14	18	F	CAVB	TdP	–	570	47	NA	NA	PM	130	None	
Ave±SD	57±21					561±76	44±11	495±42	64±27		102±71		

AVB, atrioventricular block; TdP, torsades de pointes; PM, pacemaker; CAVB, complete atrioventricular block; NA, not available; ICD, implantable cardioverter defibrillator; BB, β-blocker; Ib, class Ib antiarrhythmic drugs; VF, ventricular fibrillation.

0.02 ms. The simulation programs were coded in C++ and implemented for personal computers.[12]

Statistical Analysis

Numerical data are presented as mean±standard error of the mean. Student's t-test was used to compare the data between different groups for electrophysiological measurement, and differences were considered significant at $P<0.05$.

Results

Clinical Characteristics of the Patients in This Study

The clinical characteristics of the 14 patients enrolled in the study are presented in **Table 1**. The mean age at the onset of AVB was 57±21 years, and 13 patients (92.8%) were females. All patients showed TdP with AVB: 10 had complete AVB, 3 had 2:1 AVB, and 1 had Wenckebach AVB. No patient had experienced syncope or ventricular arrhythmias prior to the appearance of TdP. One patient (case 6 in **Table 1**) with Wenckebach AVB had 2 family members who had suddenly died at the age of 1 year and 3 months, respectively. The mother of case 12 (**Table 1**) had atrial fibrillation, mitral regurgitation, and complete AVB with prolonged QT interval, but no TdP.

In most patients with AVB-related TdP, the tachyarrhythmia started from premature ventricular contractions after a long-pause interval following ventricular arrhythmias, so-called "TdP from short–long–short pattern" (**Figure 1D**).[13] The ECGs available at the time of AVB showed severely prolonged QT interval (heart rate 44±11 beats/min and QTc 561±76 ms). On the other hand, the ECGs without AVB available in 7 cases also showed a prolonged QT interval (heart rate 64±27 beats/min, $P<0.05$, and QTc 495±42 ms, P=NS, vs those in AVB). ECGs in sinus rhythm were obtained in 4 and 3 patients before and after AVB, respectively.

All patients underwent implantation of either an implantable cardioverter-defibrillator (ICD) or permanent pacemaker (PM), together with the administration of several drugs, including β-blockers (ICD n=3; PM n=11). Mean clinical follow-up during advanced therapy was 102±71 months. After the placement of a PM or ICD, 2 patients maintained own ventricular beats but the other 12 depended on ventricular pacing during the follow-up period. Three patients had recurrence of TdP even while receiving treatment. Patient no. 11 suddenly experienced repetitive TdP because of pacing failure and no. 13 also experienced TdP when her own ventricular beats had been set faster than the basal pacing rate. In patient 6, the reappearance of Wenckebach AVB without ventricular pacing caused ventricular tachycardia. In all 3 cases, no gene mutations were detected.

Molecular Genetics and Clinical Characteristics of Patients With Gene Mutations

The genetic analysis revealed different heterozygous mutations in 4 (28.6%) of 14 AVB-related TdP cases (**Table 1**): 1 *KCNQ1* mutation, G272V, and 3 *KCNH2* mutations, D111V, A490T and P846T (**Figure 1A**). All were located in the nonpore regions; G272V is located in the S5 domain for the *KCNQ1* channel; D111V, A490T, and P846T are located in the N-terminus, S2–S3 inner loop, and C-terminal domains for the *KCNH2* channel, respectively (**Figure 1B**). In the remaining 10 patients, we were unable to detect any mutations associated with the 5 major LQTS-related genes.

G272V in *KCNQ1* (Case 7 in Table 1) The G272V muta-

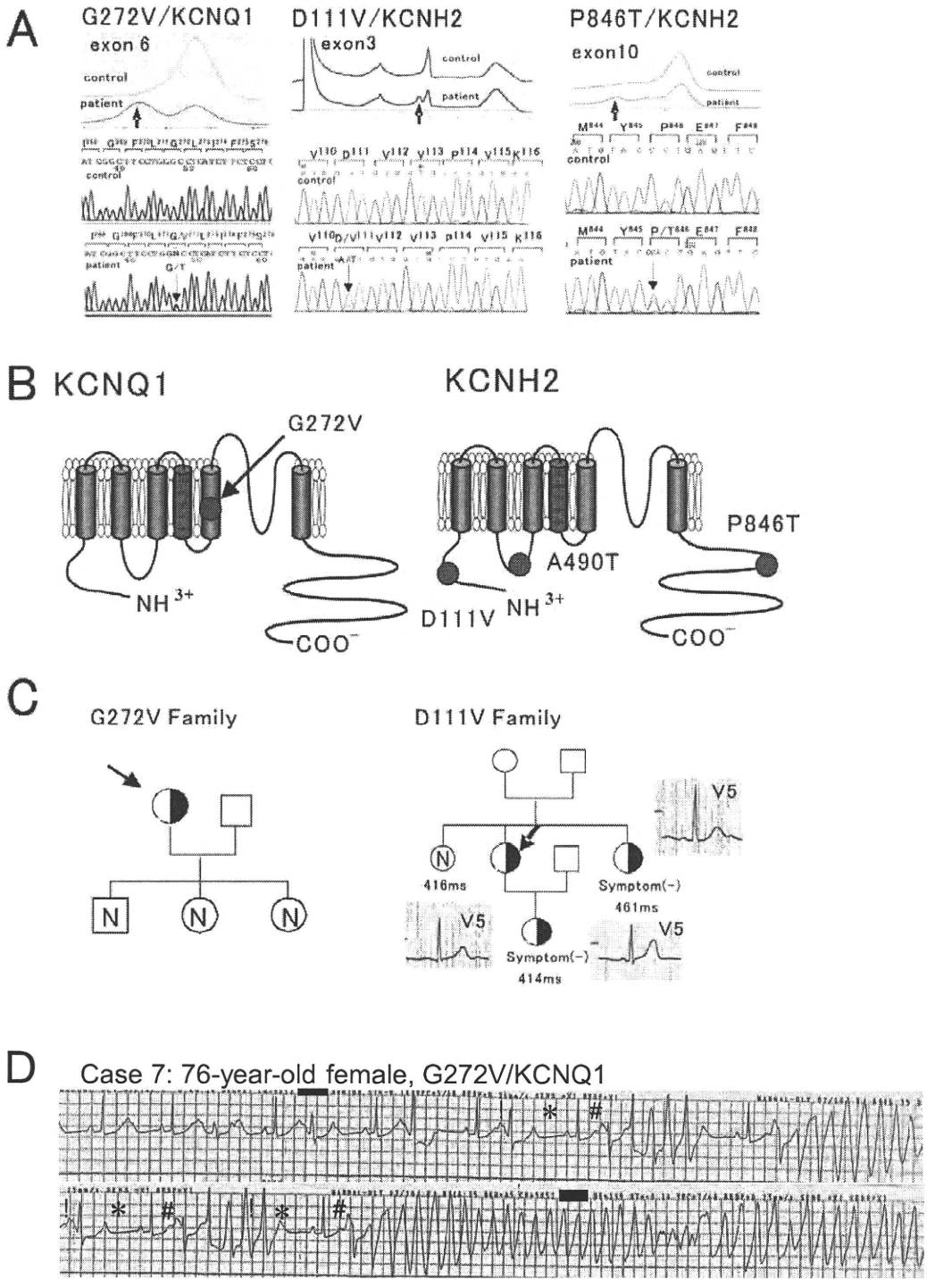

Figure 1. Molecular discovery and clinical data associated with *KCNQ1* and *KCNH2* mutations, and the initiation of atrioventricular block -related torsades de pointes (TdP). (**A**) Denaturing high-performance liquid chromatography patterns and DNA sequence data in normal controls and patients with G272V for *KCNQ1* (**Left**), D111V for *KCNH2* (**Middle**), and P846T for *KCNH2* (**Right**). (**B**) Schemes showing the topology of cardiac ion channel proteins for *KCNQ1* and *KCNH2* and the location of mutations identified in this study. (**C**) Two pedigrees of G272V and D111V families. Circles and squares represent female and male family members, respectively; probands are indicated by arrows. Heterozygous carriers are represented as half-filled symbols, family members in whom no genetic data were available are shown by open symbols, and non-carriers by open symbols with N. QTc intervals corrected by Bazzet's formula in lead V5 are given for each available family member. (**D**) Representative ECG recordings from case 7 (76-year-old female with G272V-KCNQ1 mutation). TdP during 2:1 AV block started with so-called "short (!)–long (∗)–short (#) pattern" which resulted in a long pause (∗).[13]

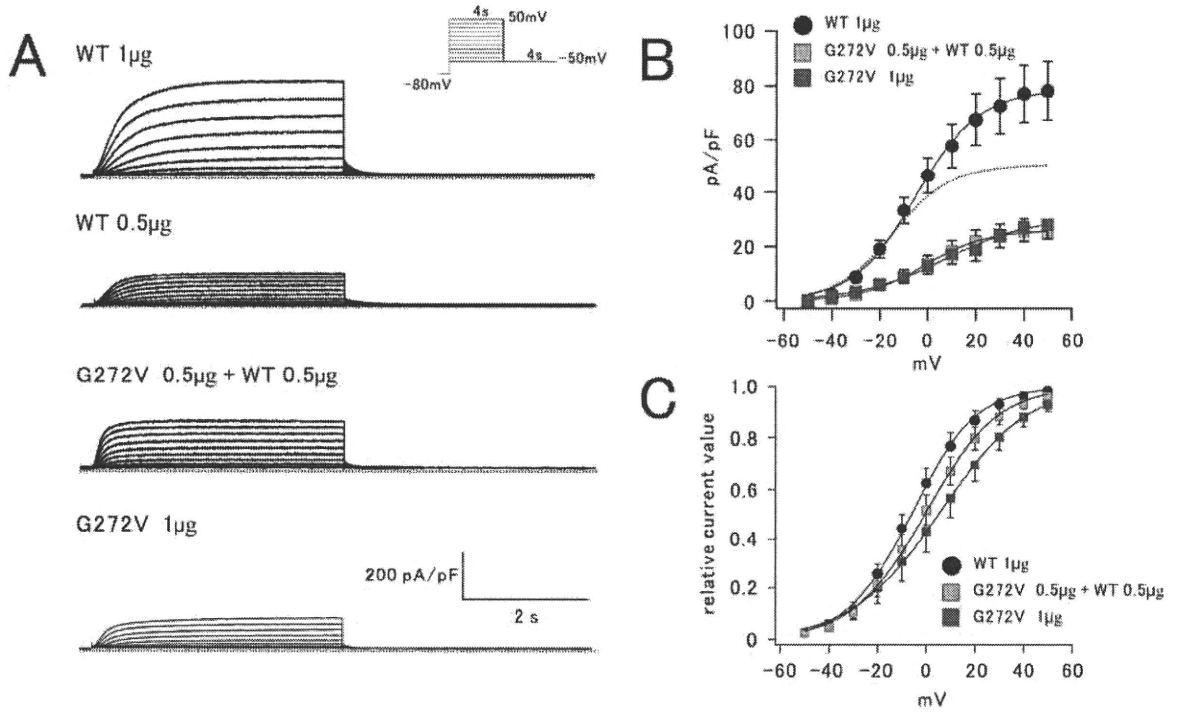

Figure 2. G272V KCNQ1 mutant channel shows loss of function associated with decreased density on I_{Ks}. Functional analyses on wild-type (WT) and G272V mutant channels expressed in Chinese Hamster ovary cells. (**A**) Representative current recordings for each channel. Currents were elicited from a holding potential of –80 mV, by depolarizing pulses (4-s duration) from –50 to +50 mV (with a 10-mV step increment) and subsequent repolarization to –50 mV for a 4-s duration (inset). Concentrations of cDNAs used for transfection are indicated near each graph. (**B**) Tail current-voltage relationships for 1 μg WT (closed circles; n=18), 0.5 μg WT (indicated by dotted line; n=14), 0.5 μg WT plus 0.5 μg G272V (green squares; n=19), 1 μg G272V (red squares; n=11). (**C**) Normalized activation curves by fitting to Boltzmann function.

tion was identified in a 76-year-old female who did not have a particularly relevant family history (**Figure 1A Left panel**). For approximately 10 years, she had taken nilvadipine and gliclazide because of hypertension and diabetes mellitus. Approximately 1 year before hospitalization, her QTc interval was within normal range (424 ms). When she was admitted to hospital because of syncope, her monitoring ECGs displayed 2:1 AVB (50 beats/min), prolonged QTc interval (578 ms), and repetitive TdP (**Figure 1D**). Her serum K^+ level was low (2.5 mEq/L). Because AVB persisted, she underwent DDD PM implantation. After correction of the serum K^+ level and PM therapy, her QTc interval shortened and TdP disappeared. She was free from cardiac events for the following 59 months. The genetic analysis revealed 3 children as non-mutation carriers (**Figure 1C Left panel**).

D111V in *KCNH2* (Case 4 in Table 1) The D111V mutation was identified in a 57-year-old female who did not have a particularly relevant family history (**Figure 1A Middle panel**). She experienced syncope after eating breakfast, and the monitoring ECG in the ambulance documented complete AVB (43 beats/min), prolonged QTc interval (525 ms) and TdP. After external PM therapy was initiated, TdP disappeared. She then underwent ICD implantation and started oral mexiletine hydrochloride (300 mg/day) and propranolol hydrochloride (30 mg/day); she has had no cardiac events over a follow-up period of 96 months. However, her QTc interval has remained prolonged even in the absence of AVB (545 ms, 4 years later). The genetic tests in her 3 relatives showed 2 mutation carriers (**Figure 1C Right panel**): a 51-year-old sister and 29-year-old daughter. Both these relatives were asymptomatic. Her daughter's QTc interval was within normal range (414 ms), but the sister's was prolonged (461 ms).

P846T in *KCNH2* (Case 8 in Table 1) The P846T mutation was found in a 71-year-old female who did not have a particularly relevant family history (**Figure 1A Right panel**). She experienced syncope after breakfast, and the monitoring ECG in the ambulance displayed complete AVB (45 beats/min) and repetitive TdP with prolonged QT interval. On admission, her AV conduction resumed at 57 beats/min, but her QTc interval remained prolonged (729 ms). After ICD implantation, she was free from cardiac events for 46 months, but her QTc interval remained prolonged (489 ms). We did not conduct a genetic analysis in this family.

A490T in *KCNH2* (Case 1 in Table 1) We have previously reported the clinical features of a A490T mutation identified in a 27-year-old female.[3] Briefly, her 12-lead ECG showed severe bradycardia because of 2:1 AVB (50 beats/min) with complete left bundle branch block and remarkable prolongation of QTc interval (600 ms). She fainted and collapsed while talking on the telephone, and the Holter ECG showed TdP associated with 2:1 AVB.

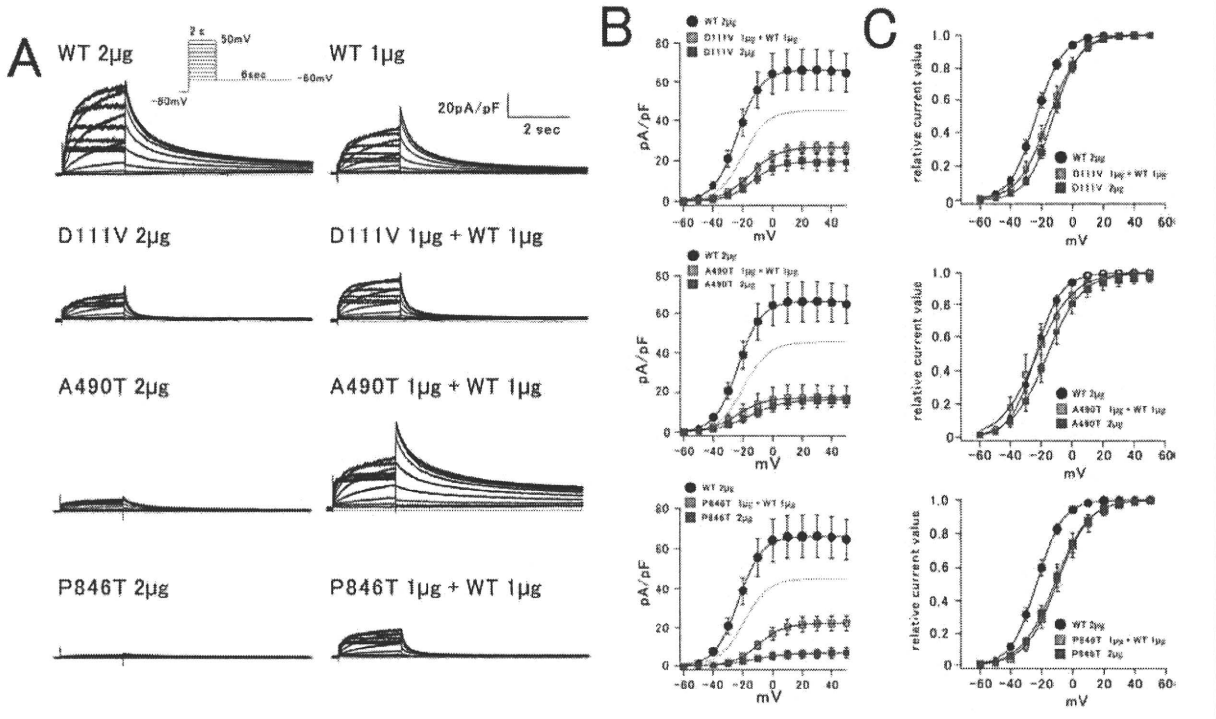

Figure 3. All *KCNH2* mutant channels show loss of function associated with decreased density on I_{Kr}. Electrophysiological characteristics of *KCNH2* mutant channels in Chinese Hamster ovary cells. (**A**) Families of representative current traces. Experimental protocol is shown in the inset. Concentrations of cDNAs used for transfection are indicated above each graph. (**B**) Tail current-voltage relationships for 2μg wild-type (WT: closed circles; n=20), 1μg WT (dotted line; n=14), 1μg WT plus 1μg mutant (green squares; n=10–13), 2μg mutant (red squares; n=8–12). (**C**) Normalized activation curves by fitting to Boltzmann function.

Table 2. Parameters of Inactivation in WT and Mutant *KCNH2*

	WT (n=16)	WT/D111V (n=16)	D111V (n=15)	WT/A490T (n=17)	A490T (n=15)	WT/P846T (n=15)	P846T (n=16)
$V_{0.5}$ (mV)	−58.3±4.7	−40.1±4.1**	−47.4±7.0	−32.5±3.9*	−44.2±3.3	−38.7±2.4**	−55.5±3.5
Slope factor	29.2±1.4	33.9±1.3	35.3±1.7**	30.6±1.4†	34.9±1.1**	33.0±0.6†	37.5±1.7*

*P<0.001 vs WT, **P<0.01 vs WT, †P<0.05 vs WT.
WT, wild-type.

Expression Study

In order to clarify the functional consequences of the G272V mutation of *KCNQ1* and the D111V, A490T, and P846T mutations of *KCNH2*, we assessed the electrophysiological properties of the WT and mutant clones by using CHO cells.

Biophysical Assay of *KCNQ1* Mutant Channel **Figure 2A** shows representative examples of whole-cell currents recorded from CHO cells transfected with WT/*KCNQ1*, G272V/*KCNQ1* alone or WT co-expressed G272V/*KCNQ1* (WT/G272V) plus *KCNE1*. CHO cells transfected with WT/*KCNQ1* (1 or 0.5μg) displayed outward currents with slow activation/deactivation kinetics on depolarization, which are typical of I_{Ks} currents, as previously reported.[14,15] In contrast, a cell transfected with G272V/*KCNQ1* (1μg) displayed smaller I_{Ks} currents compared with that of the WT (1μg). WT/G272V at an equimolar ratio (0.5μg) also showed smaller I_{Ks} currents.

In **Figure 2B**, the tail current densities at −50 mV measured in multiple cells are plotted as a function of test pulse voltages (between −50 and +50 mV). The tail current densities at −50 mV after depolarizing test pulses to +40 mV were 77.0±11 pA/pF for 1μg WT (n=18), 49.5±7.9 pA/pF for 0.5μg WT (n=14), 25.4±4.5 pA/pF for 0.5μg WT/G272V (n=19) (vs WT 1μg, P<0.001), 26.7±4.9 pA/pF for 1μg G272V (n=11) (vs WT 1μg, P<0.01). Thus, compared with the WT I_{Ks} current, co-transfection of the mutant affected the expressed current densities.

Figure 2C represents the voltage-dependence of current activation. Tail current densities after each test potential were fitted to a Boltzmann function (see Methods). The parameters were $V_{0.5}$=−5.2±3.0 mV, k=11.1±0.6 for 1μg WT, $V_{0.5}$=−1.0±3.7 mV, k=11.7±1.1 for 0.5μg WT/G272V, $V_{0.5}$=5.7±5.4 mV, k=14.3±1.6 (vs WT 1μg; P<0.05) for 1μg G272V. Regarding half-activation voltages, WT plus G272V and G272V tended to shift to the depolarization side compared with WT but there was no statistical significance. In

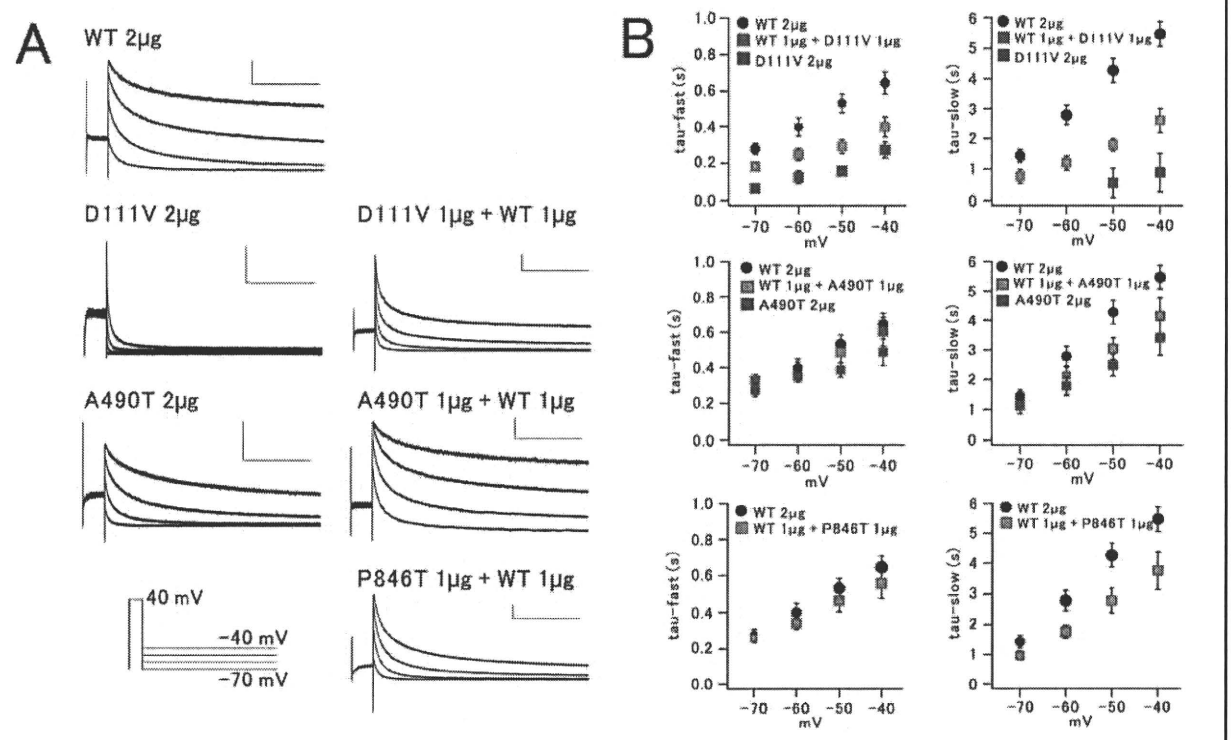

Figure 4. *KCNH2* mutant channels show a faster deactivation. (**A**) Representative tail currents elicited after depolarization to +40 mV (inset protocol). (**B**) Deactivation process was fitted to 2 components having different time constants, tau-fast and tau-slow. They were calculated in a pooled data from multiple cells transfected by 3 mutants (from top of panel B, D111V, A490T and P846T, respectively) and are plotted against membrane potentials (–70 to –40), for 2 μg WT (closed circles; n=15), 1 μg WT plus 1 μg mutant (green squares; n=7–14 for each channel), 2 μg mutant (red squares; n=6–8).

slope factors, G272V alone channel was larger than WT ($P<0.05$). Overall, the most important finding was the dominant-negative effect for the G272V channel.

Biophysical Assay of 3 *KCNH2* Mutant Channels **Figure 3A** shows representative examples of whole-cell currents recorded from CHO cells transfected with WT/*KCNH2* (2 and 1 μg), mutant/*KCNH2* (2 μg), or WT co-expressed mutant/*KCNH2* (WT/mutant) (1 μg each). CHO cells transfected with WT/*KCNH2* (2 or 1 μg, **Figure 3A Upper 2 panels**) displayed outward currents with inward rectifying properties, which are typical of I_{Kr} currents.[16] In contrast, the magnitude of currents from cells expressing all of the WT/mutants and mutant only were remarkably reduced (**Figure 3A Lower 6 panels**).

In **Figure 3B**, the tail current densities at –60 mV are plotted as a function of test pulse voltages (between –60 and +50 mV). The mean current densities after depolarizing test pulse to +20 mV in WT channels were 66.2±11 pA/pF for 2 μg (n=20) and 45.0±9.3 pA/pF for 1 μg (n=14). In contrast, those in the WT/mutant and mutant channels were 25.1±2.9 pA/pF in WT/D111V (n=13), 15.8±6.0 pA/pF in WT/A490T (n=10), 20.5±3.9 pA/pF in WT/P846T (n=12), 18.8±3.6 pA/pF for D111V (n=9), 15.2±3.4 pA/pF for A490T (n=12), 6.1±2.3 pA/pF for P846T (n=8), respectively. They were all significantly smaller than those of the 2-μg WT channels (vs WT 2 μg; $P<0.01$). **Figure 3C** shows that all WT/mutant and mutant channels tended to shift to the depolarization side compared with the WT. Overall, all mutant channels showed loss of function associated with a dominant-negative effect and shift of the activation curve to depolarization.

We then examined whether the mutations affected the inactivation kinetics of mutant channels using a double-pulse protocol. $V_{0.5}$ and the slope factor of steady-state inactivation differed between WT and WT plus mutant or mutant. All mutant *KCNH2* channels showed the shift of inactivation curves to depolarizing direction, and the differences were statistically significant (**Table 2**). Therefore, we also changed the parameters associated with inactivation states in the following simulation study.

Figure 4A depicts original current traces showing deactivation at 4 different repolarization potentials (from –70 to –40 mV) of WT and/or mutant/*KCNH2*. Deactivating currents were best fit with a double-exponential function, and are summarized in **Figure 4B**. At 4 different potentials, both time constants (Tau-fast and Tau-slow) for D111V and WT/D111V were smaller than those of the WT. Tau-slow of WT/P846T was also smaller than those of the WT. We could not assess that of P846T (2 μg), because it was too small to measure. In contrast, there were no significant changes between the WT and WT/A490T or A490T in the deactivation process.

Computer Simulation of APD

In order to compare how functional changes caused by mutations affect ventricular action potentials, a simulation study

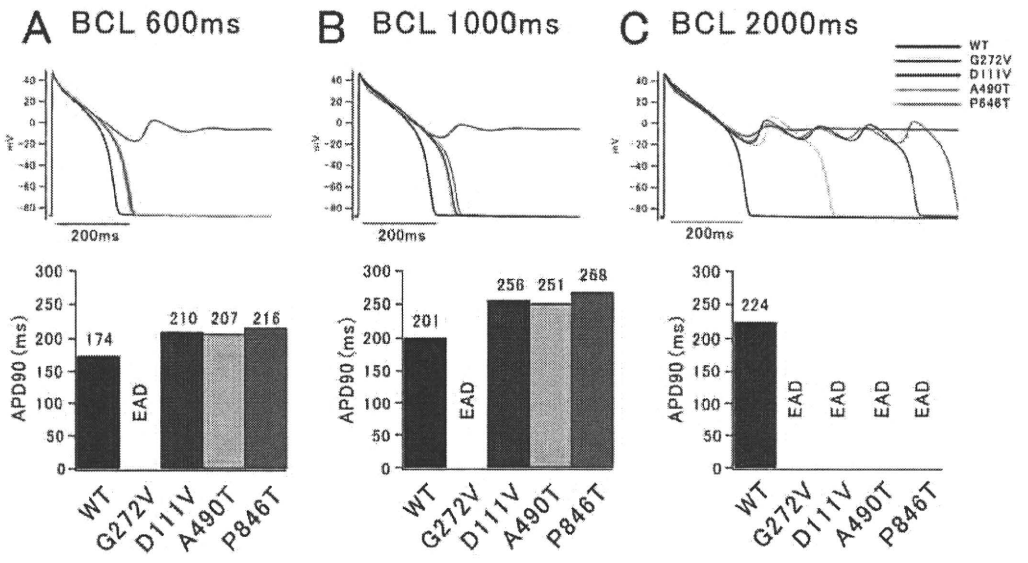

Figure 5. Computer simulations with Luo-Rudy myocardial model show bradycardia-induced early afterdepolarization (EAD). Each figure presents (**A**) action potential duration (APD) at basic cycle length (BCL) of 600 ms, (**B**) APD at BCL of 1,000 ms, and (**C**) APD at BCL of 2,000 ms. The longer the BCL in each model was, the more the APD was prolonged. EADs appeared in the models of D111V/WT, A490T/WT, and P846T/WT only at BCL of 2,000 ms, but appeared at all BCLs in the case of G272V/WT.

Table 3. Parameters of Simulation Data in Bradycardia-Induced Long QT Syndrome

Gene	Mutation	WT basal parameters	Mutant changed parameters
KCNQ1	G272V	gsk=0.202*(1+0.6/(1+pow(0.000038/cai),1.4)))	gsk=0.067*(1+0.6/(1+pow(0.000038/cai),1.4)))
		xs1 ss=1/(1+exp(-(v-1.5)/16.7))	xs1 ss=1/(1+exp(-(v-6.5)/16.7))
KCNH2	D111V	gherg=0.0135*pow(Kout,0.59)	gherg=0.331*0.0135pow(Kout,0.59)
		$\alpha\alpha$=65.5e-3*exp(0.05547153*(v-36))	$\alpha\alpha$=65.5e-3*exp(0.05547153*(v-69))
		αi=0.439*exp(–0.02352*(v+25))*4.5/Kout	αi=0.439*exp(–0.02352*(v+3))*4.5/Kout
		$\beta\beta$=2.9375e-3*exp(–0.02158*v)	$\beta\beta$=2*2.9375e-3*exp(–0.02158*v)
KCNH2	A490T	gherg=0.0135*pow(Kout,0.59)	gherg=0.1887*0.0135pow(Kout,0.59)
		αi=0.439*exp(–0.02352*(v+25))*4.5/Kout	αi=0.439*exp(–0.02352*(v-6))*4.5/Kout
KCNH2	P846T	gherg=0.0135*pow(Kout,0.59)	gherg=0.265*0.0135pow(Kout,0.59)
		$\alpha\alpha$=65.5e-3*exp(0.05547153*(v-36))	$\alpha\alpha$=65.5e-3*exp(0.05547153*(v-80))
		αi=0.439*exp(–0.02352*(v+25))*4.5/Kout	αi=0.439*exp(–0.02352*(v+3))*4.5/Kout
		$\beta\beta$=2.9375e-3*exp(–0.02158*v)	$\beta\beta$=1.3*2.9375e-3*exp(–0.02158*v)

was conducted using the Luo-Rudy model, which incorporated the Markov[13] or Hodgkin-Huxley[17] process gating for the mutant channels (**Figure 5**). **Table 3** shows the parameters of simulation that were changed to fit to experimental results. We simulated action potentials in all myocardial layers at 3 different basic cycle lengths (BCL 600, 1,000, 2,000 ms) (**Figures 5A–C**). In the endocardium and epicardium, APD of all mutant models was prolonged, but did not produce early afterdepolarizations (EAD) (data not shown in **Figure 5**). In contrast, in the simulated M cell layer, APD was lengthened significantly at a slower heart rate. In the lower half of **Figure 5**, below each simulated action potential, the corresponding bar graphs show APDs at 90% repolarization. Three APD models with D111V, A490T, and P846T displayed EADs at BCL of 2,000 ms, whereas G272V displayed it at all BCLs.

Discussion

There are 3 major findings in the present study. (1) In 4 of 14 consecutive AVB-associated TdP patients, 3 *KCNH2* and 1 *KCNQ1* heterozygous missense mutations were identified. (2) Electrophysiological analyses revealed loss of function associated with decreased current densities and various dysfunctions on I_{Ks} or I_{Kr} in 4 mutants. (3) Functional changes reconstituted by the computer simulation resulted in a prolonged APD and EAD under condition of bradycardia.

During AVB, our 14 patients showed a prolonged QT interval and TdP. Based on a comparison of ECGs available before and after AVB, we found the QT intervals were lengthened even in the absence of AVB. These clinical characteristics indicate that AVB-related TdP might share a similar genetic background with congenital LQTS: mutations on cardiac ion channel genes could be partially causative. Lupo-

glazoff et al[5] demonstrated that in neonates that, while LQTS with 2:1 AVB is associated with *KCNH2* mutations, sinus bradycardia-related LQTS is associated with *KCNQ1* mutations. In 9 of 10 cases, 2:1 AVB-induced LQTS could be caused by LQTS-related gene mutations. In contrast, Chevalier et al found 4 K^+ channel gene mutations in 5 of 29 adult patients with AVB-induced LQTS (17.3%).[6] Our cohort also consisted of adult LQTS patients, with a mutation rate of 28.6%. This prevalence rate was similar to Chevalier's report, but lower than that in the 2:1 AVB-related LQTS in neonates. These studies have shown that AVB-induced LQTS in neonates has a stronger genetic association than AVB-induced LQTS in adults. Regarding the diagnostic rate of genetic testing in general, no candidate mutations could be detected in 30–40% of congenital LQTS cases. In contrast, it has been shown recently that genetic polymorphisms modify the QT interval.[18–24] Although we did not check polymorphisms in the present study, it is possible that our subjects might have some modifier-gene mutations. Thus, it remains possible that the remaining 10 patients in our study without apparent genetic variants may have as yet unknown variants.

In our cohort, it was difficult to prove the efficacy of β-blockers because very few patients were taking these drugs. In order to investigate the efficacy of β-blockers it will be necessary to study more cases with AVB-induced TdP. The first step in the treatment of all patients with AVB-induced TdP is the implantation of a device. Although PM implantation as first-line therapy for AVB-induced TdP is not disputed, 3 of our patients had a recurrence of TdP after the device was implanted, because of inadequate ventricular pacing, suggesting that AVB patients with TdP require strict PM management. In cases of persistent QT prolongation, even after PM therapy, it might become necessary to consider ICD implantation.

Several AVB-related gene mutations have been functionally assayed:[6] 3 *KCNH2* mutations, R328C, R696C and R1047L, were shown to have no strong dominant-negative effects on I_{Kr}. Another *KCNE2* mutation (R77W), which was identified in an AVB patient while taking flecainide, exerted no effects on I_{Kr}. Overall, previous analyses of mutations have shown them to cause only mild functional change. Our study showed similar results; all 4 mutants displayed loss of function associated with decreased densities on I_{Ks} or I_{Kr}, which were basically similar to those in congenital LQTS. On average, our patients experienced TdP at 57 years of age, which is older than the mean age of onset reported for those with congenital LQTS. Mutation carriers, who remain asymptomatic well into adulthood, may incidentally have fatal events in the presence of additional triggers, such as AVB.[25]

Several mutations of *SCN5A,* coding the α-subunit of Na^+ channels, have been found in newborn and infant cases of long QT.[26–28] They showed functional 2:1 AVB caused by profound QT prolongation. Therefore, the pathological basis differs between those cases and ours. Irrespective of genetic testing results, our patients who developed TdP in the presence of AVB showed QT prolongation, even in sinus rhythm. Thus, AVB may not be directly associated with QT prolongation, but the bradycardia caused by AVB enhances it and eventually leads to TdP. Our computer simulation study showed that, at a slower heart rate, APD lengthened significantly, suggesting that AVB-related bradycardia could exacerbate QT prolongation.

Study Limitation

Female sex is a predisposing factor for the development of cardiac arrhythmic events in patients with congenital and acquired LQTS, as previous reports have demonstrated.[29–31] In our study, almost all patients (93%) were also female, and therefore it would be possible that not only AVB but female sex affected cardiac repolarization and ventricular irritability in our cohort.

Conclusion

This study showed that incidental AVB as a trigger of TdP could manifest as clinical phenotypes of LQTS, and that some patients with AVB-induced TdP could have genetic backgrounds associated with congenital LQTS-related genes.

Acknowledgments

We thank Ms Arisa Ikeda for excellent technical assistance. This work was supported by a Grant-in-Aid for Scientific Research from the Japan Society for the Promotion of Science and the Biosimulation and Health Sciences Research Grant from the Ministry of Health, Labor, and Welfare of Japan, and grants from the Uehara Memorial Foundation (M.H.) and the Grant-in-Aid for Young Scientists from the Ministry of Education, Culture and Technology of Japan (H.I.).

References

1. Moss A, Kass R. Long QT syndrome: From channels to cardiac arrhythmias. *J Clin Invest* 2005; **115:** 2018–2024.
2. Shimizu W. Clinical Impact of Genetic Studies in Lethal Inherited Cardiac Arrhythmias. *Circ J* 2008; **72:** 1926–1936.
3. Kurita T, Ohe T, Marui N, Aihara N, Takaki H, Kamakura S, et al. Bradycardia-induced abnormal QT prolongation in patients with complete atrioventricular block with torsades de pointes. *Am J Cardiol* 1992; **69:** 628–633.
4. Yoshida H, Horie M, Otani H, Kawashima T, Onishi Y, Sasayama S. Bradycardia-induced long QT syndrome caused by a de novo missense mutation in the S2-S3 inner loop of HERG. *Am J Med Genet* 2001; **98:** 348–352.
5. Lupoglazoff JM, Denjoy I, Villain E, Fressart V, Simon F, Bozio A, et al. Long QT syndrome in neonates: Conduction disorders associated with HERG mutations and sinus bradycardia with KCNQ1 mutations. *J Am Coll Cardiol* 2004; **43:** 826–830.
6. Chevalier P, Bellocq C, Millat G, Piqueras E, Potet F, Schott JJ, et al. Torsades de pointes complicating atrioventricular block: Evidence for a genetic predisposition. *Heart Rhythm* 2007; **4:** 170–174.
7. Nagaoka I, Shimizu W, Itoh H, Yamamoto S, Sakaguchi T, Oka Y, et al. Mutation site dependent variability of cardiac events in Japanese LQT2 form of congenital long-QT syndrome. *Circ J* 2008; **72:** 694–699.
8. Makita N. Phenotypic overlap of cardiac sodium channelopathies. *Circ J* 2009; **73:** 810–817.
9. Ogawa K, Nakamura Y, Terano K, Ando T, Hishitani T, Hoshino K. Isolated non-compaction of the ventricular myocardium associated with long QT syndrome. *Circ J* 2009; **73:** 2169–2172.
10. Bazett HC. An analysis of the time relations of electrocardiograms. *Heart* 1920; **7:** 353–370.
11. Clancy CE, Rudy Y. Na^+ channel mutation that causes both Brugada and long-QT syndrome phenotypes: A simulation study of mechanism. *Circulation* 2002; **105:** 1208–1213.
12. Itoh H, Sakaguchi T, Ding WG, Watanabe E, Watanabe I, Nishio Y, et al. Latent genetic background and molecular pathogenesis of drug-induced long QT syndrome. *Circ Arrhythmia Electrophysiol* 2009; **2:** 511–523.
13. Tan HL, Bardai A, Shimizu W, Moss AJ, Schulze-Bahr E, Noda T, et al. Genotype-specific onset of arrhythmias in congenital long-QT syndrome. *Circulation* 2006; **114:** 2096–2103.
14. Barhanin J, Lesage F, Guillemare E, Fink M, Lazdunski M, Romey G. KvLQT1 and lsK (minK) proteins associate to form the I_{Ks} cardiac potassium current. *Nature* 1996; **384:** 78–80.
15. Sanguinetti MC, Curran ME, Zou A, Shen J, Spector PS, Atkinson DL, et al. Coassembly of KvLQT1 and minK (I_{sK}) proteins to form cardiac I_{Ks} potassium channel. *Nature* 1996; **384:** 80–83.
16. Sanguinetti MC, Jiang C, Curran ME, Keating MT. A mechanistic link between an inherited and an acquired cardiac arrhythmia: *HERG* encodes the I_{Kr} potassium channels. *Cell* 1995; **81:** 299–307.